PCCP

PAPER

View Article Online
View Journal | View Issue

Cite this: *Phys. Chem. Chem. Phys.*, 2014, **16**, 7980

Microsolvation of the acetanilide cation (AA^+) in a nonpolar solvent: IR spectra of AA^+–L_n clusters (L = He, Ar, N_2; $n \leq 10$)†

Matthias Schmies,[a] Alexander Patzer,[a] Markus Schütz,[a] Mitsuhiko Miyazaki,[b] Masaaki Fujii[b] and Otto Dopfer*[a]

Received 27th January 2014,
Accepted 24th February 2014

DOI: 10.1039/c4cp00401a

www.rsc.org/pccp

Infrared photodissociation (IRPD) spectra of mass-selected cluster ions of acetanilide (*N*-phenylacetamide), AA^+–L_n, with the ligands L = He (n = 1–2), Ar (n = 1–7), and N_2 (n = 1–10) are recorded in the hydride stretch (amide A, ν_{NH}, ν_{CH}) and fingerprint (amide I–III) ranges of AA^+ in its $^2A''$ ground electronic state. Cold AA^+–L_n clusters are generated in an electron impact ion source, which predominantly produces the most stable isomer of a given cluster ion. Systematic vibrational frequency shifts of the N–H stretch fundamentals (ν_{NH}) provide detailed information about the sequential microsolvation process of AA^+ in a nonpolar (L = He and Ar) and quadrupolar (L = N_2) solvent. In the most stable AA^+–L_n clusters, the first ligand forms a hydrogen bond (H-bond) with the N–H proton of *trans*-AA^+ (*t*-AA^+), whereas further ligands bind weakly to the aromatic ring (π-stacking). There is no experimental evidence for complexes with the less stable *cis*-AA^+ isomer. Quantum chemical calculations at the M06-2X/aug-cc-pVTZ level confirm the cluster growth sequence derived from the IR spectra. The calculated binding energies of D_e(H) = 720 and 1227 cm^{-1} for H-bonded and D_e(π) = 585 and 715 cm^{-1} for π-bonded Ar and N_2 ligands in *t*-AA^+–L are consistent with the observed photofragmentation branching ratios of AA^+–L_n. Comparison between charged and neutral $AA^{(+)}$–L dimers indicates that ionization switches the preferred ion–ligand binding motif from π-stacking to H-bonding. Electron removal from the HOMO of AA^+ delocalized over both the aromatic ring and the amide group significantly strengthens the C=O bond and weakens the N–H bond of the amide group.

1. Introduction

The intermolecular interaction of aromatic molecules with surrounding solvent molecules plays an important role in chemical and biological recognition.[1–3] A molecular-level understanding of these phenomena requires the knowledge of the intermolecular potential energy surface describing the interaction between aromatic molecules and the solvating ligands. It is well established that the fruitful combination of spectroscopy and quantum chemical techniques applied to isolated and size-selected clusters provides direct access to this potential.[3–11]

In these A–L_n clusters, the aromatic chromophore (A) can be solvated by a well-defined and adjustable number (n) of ligands (L). Here, we investigate the interaction of the acetanilide (AA, *N*-phenylacetamide, C_8H_9N, Fig. 1) cation with He, Ar, and N_2 ligands in the size range $n \leq 10$ to probe the initial steps of the microsolvation process of this elementary ion in a nonpolar and quadrupolar solvent. Acetanilide is the simplest aromatic amide with a –NH–CO– peptide linkage, in this case connecting a phenyl with a methyl group. Hence, AA is frequently used as a model system to characterize the biophysically relevant interaction of aromatic peptides with their surrounding environment. In addition, AA and its derivatives, such as paracetamol or phenacetin, are important drug components in pharmaceutical applications.[12]

The $AA^{(+)}$–L_n complexes with L = He, Ar, and N_2 studied in the present work belong to the class of acidic aromatic molecules interacting with nonpolar ligands. Such aromatic molecules with acidic functional groups, here the N–H bond of the amide group, offer at least two competing principal ligand binding sites, namely hydrogen bonding to the acidic group (H-bond) and π-stacking to the aromatic ring (π-bond). In the

[a] *Institut für Optik und Atomare Physik, Technische Universität Berlin, Hardenbergstr. 36, 10623 Berlin, Germany. E-mail: dopfer@physik.tu-berlin.de; Fax: +49 30-31423018*

[b] *Chemical Resources Laboratory, Tokyo Institute of Technology, Yokohama 226-8503, Japan*

† Electronic supplementary information (ESI) available: (1–2) Molecular orbitals and NBO charge distributions of *t*/*c*-AA^+; (3–5) IRPD spectra of AA^+–Ar_n, AA^+–$(N_2)_n$, and *t*-AA–Ar in hydride stretch range; (6–9) IRPD spectra of AA^+–Ar_n, AA^+–$(N_2)_n$, and *t*-AA–Ar in fingerprint range; (10) EI-IR and REMPI-IR spectra of AA^+–Ar_{1-2}. See DOI: 10.1039/c4cp00401a

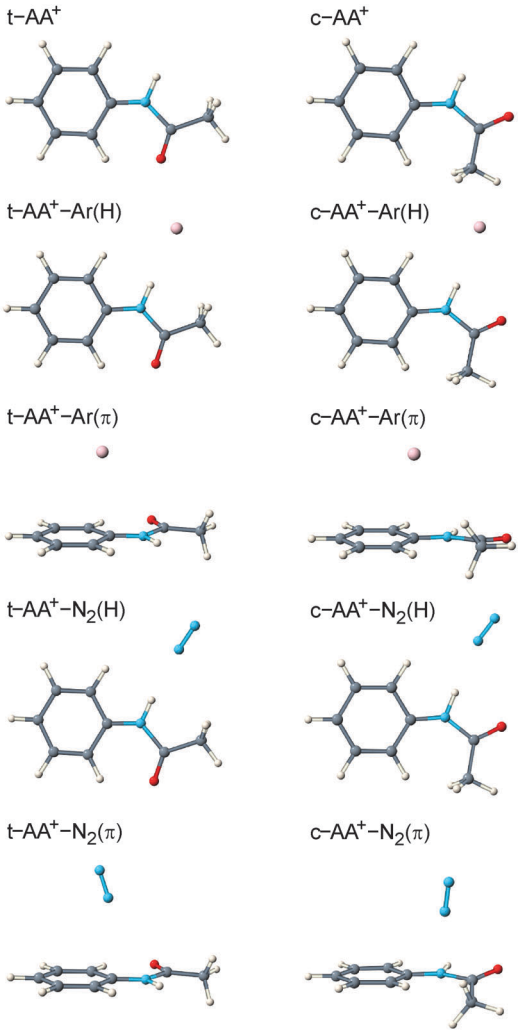

Fig. 1 Structures of *c*/*t*-AA^+ and *c*/*t*-AA^+–L dimers with L = Ar and N_2 obtained at the M06-2X/aug-cc-pVTZ level. Relevant structural, vibrational, and energetic parameters are listed in Table 1.

past, spectroscopic and quantum chemical studies have demonstrated that such A–L dimers usually prefer π-bonds in the neutral ground electronic state (S_0), because dispersion forces between L and the highly polarizable aromatic π-electron system of A dominate the attraction. In contrast, the corresponding A^+–L dimer cations usually prefer H-bonds with the acidic functional group(s) due to additional charge-induced interactions arising from the excess charge.[9,13] This ionization-induced π → H switch in the preferred $A^{(+)}$–L binding motif has recently been established *via* the combination of IR spectroscopy and quantum chemical calculations for a variety of acidic aromatic molecules interacting with rare gas (Rg) atoms, CH_4, and N_2,[9] including (substituted) phenols,[13–22] naphthol,[23] aniline,[24–26] aminobenzonitrile,[27,28] imidazole,[29,30] indole,[31] and tryptamine.[32] In some of these clusters, this ionization-induced π → H switch triggers an intermolecular isomerization reaction upon photoionization, which occurs on the picosecond timescale[33–35] and is usually inferred from IR spectra recorded before and after ionization using nanosecond laser systems. For the prototypical phenol$^{(+)}$–Rg_n clusters (Rg = Ar, Kr), this π → H rearrangement reaction has recently been monitored in real time by picosecond time-resolved IR spectroscopy, providing for the first time experimental data for intermolecular solvent dynamics in isolated clusters.[33,36–39] For $AA^{(+)}$–L_n clusters with L = Rg and N_2, a similar π → H switch in the preferred ligand binding site has been anticipated but the only available preliminary IR spectra for L = Ar with $n \leq 2$ were not conclusive.[40]

Acetanilide can occur in two different conformations (Fig. 1), namely the more stable *trans* isomer (*t*-AA, *anti*) and the significantly less stable *cis* isomer (*c*-AA, *syn*). Whereas nearly all previous studies report the detection of merely the *t*-AA isomer in both the condensed[41,42] and the gas phase,[40,43–46] the *c*-AA isomer has only recently been identified for the first time in the ground electronic state (S_0) by rotational spectroscopy in a molecular beam.[47] From the observed population ratio of ~15, the difference in relative Gibbs energy between *c*-AA and *t*-AA could be estimated as $\Delta G_{298} = 550\ cm^{-1}$, in good agreement with available quantum chemical calculations.[47] Microwave,[43,47] IR,[40,44] and electronic[40,44–46] spectra reveal that isolated *t*-AA has a "planar" equilibrium structure with C_s symmetry with all heavy atoms of the phenyl ring and the methylated amide group lying in the molecular plane, in line with quantum chemical predictions.[43,44,46,47] One of the H atoms of the CH_3 group faces the C=O bond in the molecular plane, although the three-fold barrier for internal methyl rotation is rather low in S_0 ($V_b < 50\ cm^{-1}$).[43,46,47] The *c*-AA isomer is well separated from the *t*-AA isomer by a large barrier and has a nonplanar equilibrium configuration, *i.e.*, the phenyl plane is twisted from the amide plane.[47]

Early low-resolution photoelectron spectra[48,49] demonstrate that the $^2A''$ ground electronic state (D_0) of the AA^+ cation is generated by removal of one electron from the HOMO, which is the π HOMO of the aromatic ring strongly mixed with the π HOMO of the acetylamino group. The analysis of the charge distribution reveals that ~0.4 *e* of the excess positive charge is localized on the methylated amide side chain,[46] confirming the conclusion of substantial conjugation between the phenyl and amide π orbitals. High-resolution zero kinetic energy photoelectron (ZEKE) spectra of *t*-AA^+ are consistent with a planar equilibrium structure with a high barrier for internal methyl rotation ($V_b \sim 300\ cm^{-1}$) and exhibit a few low-frequency Franck–Condon active vibrational modes ($<1000\ cm^{-1}$).[46] However, no spectroscopic information is available about the amide I–III and N–H stretch modes (amide A), which are sensitive to secondary structures in proteins. There is also essentially no spectroscopic and theoretical information available for the *c*-AA^+ isomer.

Here, we report IR spectra and quantum chemical calculations of AA^+–L_n clusters with L = He ($n \leq 2$), Ar ($n \leq 7$), and N_2 ($n \leq 10$) in the hydride stretch and fingerprint ranges. This cluster system was selected for the following reasons. Very limited spectroscopic information is available for AA^+ and its clusters with nonpolar and polar ligands. The ZEKE spectra of the *t*-$AA^{(+)}$–Ar dimer obtained *via* resonance-enhanced two-photon ionization (REMPI) were interpreted with a π-bonded

equilibrium structure in the neutral $S_{0/1}$ and cationic D_0 states, denoted *t*-$AA^{(+)}$–$Ar(\pi)$.[50] Ar complexation at the π-site was found to have little influence on the CH_3 internal rotation barrier. Intermolecular bending frequencies in the D_0 state were measured as β_x = 12 and β_y = 18 cm^{-1}.[50] Preliminary IR photodissociation (IRPD) spectra of *t*-AA^+–Ar_n (n = 1–2) clusters generated by REMPI exhibit in the N–H stretch range (ν_{NH}) doublet absorptions near 3370 cm^{-1} but the geometry of the complexes could not be assigned and the origin of the splitting (~10 cm^{-1}) remained unclear.[40] In the current study, AA^+–Ar_n clusters are generated in an electron ionization (EI) source, which generates predominantly the most stable isomer of a given cluster ion.[9,13] Significantly, the IRPD spectrum of AA^+–Ar generated by EI demonstrates unambiguously that the H-bonded *t*-AA^+–Ar(H) dimer, in which Ar binds to the acidic N–H bond of the amide group, is in fact more stable than the *t*-AA^+–$Ar(\pi)$ isomer previously identified by REMPI techniques.[40,50] Moreover, the splitting in the N–H stretch range observed previously will be assigned to the ν_{NH} fundamentals of the *t*-AA^+–Ar(H) and *t*-AA^+–$Ar(\pi)$ isomers. So far, no information is available for AA^+–Ar_n with $n \geq 3$ and AA^+–$(N_2)_n$ clusters. Thus, the presented IRPD spectra provide for the first time a reliable impression on the microsolvation process of AA^+ in a nonpolar and quadrupolar solvent, in particular with respect to the competition between various intermolecular binding motifs including H-bonding and π-stacking. Spectra are recorded in the hydride stretch (2800–3600 cm^{-1}) and fingerprint range (700–1900 cm^{-1}), covering the important amide A and I–III bands, which are sensitive to secondary protein structure. Comparison with the H-bonded *t*-AA^+–H_2O and *t*-AA^+–CH_3OH dimers characterized previously by ZEKE[51] and IRPD[34,40,52] spectroscopy will reveal the differences in the interaction of *t*-AA^+ with polar and nonpolar ligands. As essentially no information is available at all for *c*-AA^+ and its clusters, we explored also their properties in order to evaluate the effects of *cis–trans* isomerization on the geometric, vibrational, and electronic structure and the stability of *c*/*t*-AA^+ and their clusters. As the EI source might produce a significant population of *c*-AA^+, its *c*-AA^+–L_n clusters may also be detected in the present experiments. Finally, the IRPD spectra of AA^+–L_n recorded in the hydride stretch and fingerprint ranges provide for the first time detailed spectroscopic information about the C–H and N–H stretch modes as well as the amide I–III modes of the bare AA^+ cation. Comparison of these data with the corresponding spectra of neutral *t*-AA[44] will provide experimental information about the effects of ionization on the geometric and vibrational structure of *t*-$AA^{(+)}$, including the important amide group.

2. Experimental and computational techniques

IRPD spectra of mass-selected AA^+–L_n cluster ions with L = He, Ar, and N_2 are recorded in a tandem quadrupole mass spectrometer coupled to an electron impact ionization source and an octopole ion trap.[9,53] Weakly bound AA^+–L_n cluster ions are produced in a pulsed supersonic plasma expansion by electron and/or chemical ionization of AA close to the nozzle orifice and subsequent clustering reactions.[15] The expanding gas mixture is produced by passing either He (15–20 bar), Ar (5–7 bar), or N_2 (4–6 bar) carrier gas through a reservoir filled with AA heated to 120–135 °C. AA was purchased from Sigma-Aldrich (>99.9% purity) and used without further purification. A typical mass spectrum of the ion source using N_2 carrier gas is shown in Fig. 2 for the mass range 50–350 u. It is dominated by X^+–$(N_2)_n$ cluster series with $X^+ = N_2^+$ and N_3^+ (with the usual strong even/odd intensity alternation),[15,24] AA^+ (m/z 135), the AA_2^+ dimer cation (m/z 270), the aniline cation as the major fragment ion of AA^+ arising from H_2CCO elimination (F^+, m/z 93),[54] and $X^+ = H_2O$ (m/z 18) arising from water impurity in the gas inlet system. In general, the abundance of AA^+–L_n clusters decreases rapidly with increasing cluster size, consistent with the formation of weakly bound clusters by sequential addition of individual ligands to the molecular ion. Although the relative intensities of AA^+–$(N_2)_n$ in Fig. 2 decrease as 30 : 6 : 5 : 4 : 3 : 2 : 1.5 : 1 for n = 0–7, IR spectra with respectable signal-to-noise ratios are obtained for these clusters, demonstrating the high sensitivity of the experimental approach. In the case of AA^+–$(N_2)_n$ clusters, the limit for obtaining IRPD spectra ($n \leq 10$) did not arise from insufficient cluster ion generation but from the upper limit of the mass range of the first quadrupole (m/z 430).

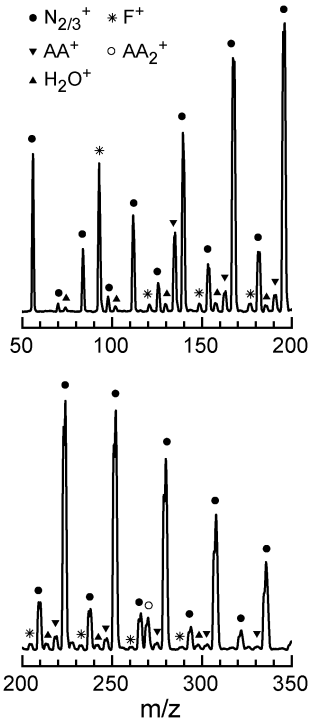

Fig. 2 Mass spectrum of the EI ion source using N_2 carrier gas, which is dominated by X^+–$(N_2)_n$ cluster series with $X^+ = N_2^+$ and N_3^+ (with the usual strong even/odd intensity alternation, filled circles), AA^+ (m/z 135, filled down triangles), the AA_2^+ dimer cation (m/z 270, open circle), the aniline cation as the major fragment ion of AA^+ arising from elimination of H_2CCO (F^+, m/z 93, asterisks),[54] and $X^+ = H_2O$ (m/z 18, filled up triangles) arising from water impurity in the gas inlet system.

AA^+–L_n ions of interest are size-selected by the first quadrupole and irradiated in an adjacent octopole with a tunable IR laser pulse (ν_{IR}) generated by an optical parametric oscillator (IR-OPO) pumped by a Q-switched nanosecond Nd:YAG laser. The IR-OPO laser is characterized by a pulse energy of ~0.3–1 and 2–5 mJ in the 1000–2000 and 2800–3500 cm^{-1} ranges, a repetition rate of 10 Hz, and a bandwidth of 1 cm^{-1}. Calibration of the IR laser frequency accurate to better than 1 cm^{-1} is accomplished using a wavemeter. Resonant excitation into vibrational resonances induces evaporation of one or several ligands, according to

$$AA^+–L_n + h\nu_{IR} \rightarrow AA^+–L_m + (n–m)L \quad (1)$$

The rupture of the weak intermolecular bonds is the only fragment channel observed. The generated AA^+–L_m fragment ions are selected by the second quadrupole and monitored by a Daly detector as a function of the laser frequency (ν_{IR}) to obtain the IRPD spectra of the AA^+–L_n parent clusters. To establish and confirm the composition of a given cluster ion, collision-induced dissociation (CID) spectra are recorded. For this purpose, the octopole is filled with N_2 up to 10^{-5} mbar, which results in collisions with ~10 eV collision energy in the laboratory frame. As an example, Fig. 3 shows mass spectra obtained by mass selecting AA^+–$(N_2)_4$ with the first quadrupole (m/z 247) and scanning the second quadrupole. The CID spectrum reveals fragmentation into all possible AA^+–$(N_2)_m$ fragment channels with m = 0–3 clearly confirming the composition of the m/z 247 ion as AA^+–$(N_2)_4$. The mass spectrum recorded without laser and collisional activation reveals little fragmentation into the m = 3 fragment channel arising from metastable decay (MD) of hot n = 4 parent clusters in the octopole region. As usually observed and in contrast to CID, MD processes lead mostly to the loss of a single ligand, indicating that the clusters produced in the EI source and probed in the octopole are rather cold. Additional fragmentation into the m = 0 and 1 channels arises from laser-induced dissociation (LID) of the n = 4 parent cluster at ν_{IR} = 3367 cm^{-1} (ν_{NH}). In general, LID leads to a narrow range of fragment channels, and this information can be used to estimate the binding energies of the ligands.[9] To separate contributions of MD from LID, the ion source is triggered at twice the laser frequency, and signals from alternating triggers are subtracted. This procedure compensates for slow variations of parent ion currents generated in the ion source. Although the IR spectra are not normalized for laser intensity fluctuations monitored by a pyroelectric detector, the relative intensities of widely spaced bands are believed to be accurate to within a factor of 2–3, mainly due to the changes in the spatial overlap between the IR laser and ion beams. The widths of the transitions in the experimental IRPD spectra of AA^+–L_n increase in the order L = He, Ar, and N_2 and decrease somewhat with the cluster size n. For example, the widths of the ν_{NH} transitions of the AA^+–L dimers are 6, 9, and 14 cm^{-1} for L = He, Ar, and N_2, respectively. The width arises mainly from unresolved rotational substructure and possibly sequence transitions involving low-frequency intermolecular modes. Thus, the widths correlate with the binding energy of the most weakly bound ligand in the complex, which determines the upper limit of the internal energy that can be deposited in the cluster.

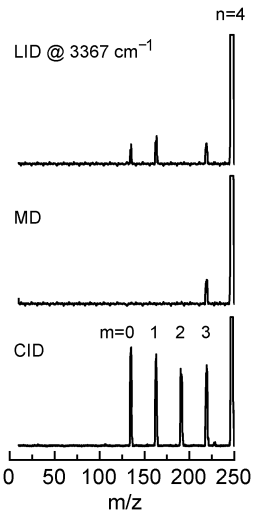

Fig. 3 Mass spectra obtained by mass-selecting the AA^+–$(N_2)_n$ parent cluster with n = 4 (off-scale, m/z 247) using the first quadrupole and scanning the second quadrupole. In the case of collision-induced dissociation (CID), fragmentation into all possible AA^+–$(N_2)_m$ fragment channels (m = 0–3) is observed. Without laser action and collision gas in the octopole, only metastable decay (MD) into the m = 3 channel is observed. Upon resonant laser excitation at ν_{IR} = 3367 cm^{-1} (ν_{NH}) additional laser-induced dissociation (LID) occurs into the m = 0 and m = 1 channels.

The geometry and vibrational frequencies of AA, AA^+, and their $AA^{(+)}$–L_n clusters are characterized at the M06-2X/aug-cc-pVTZ level[55] to support the vibrational and isomer assignments and to investigate the effects of ionization and complexation on the geometric, vibrational, and electronic structure. Initial calculations at the UMP2/6-311+G(d,p) level revealed rather high spin contamination for the open-shell t-AA^+ radical cation in its $^2A''$ ground electronic state (*e.g.*, $\langle S^2\rangle - 0.75 = 0.28$ and 0.06 before and after annihilation). Hence, the MP2 level was not considered suitable for a reliable description of AA^+ and its weak interaction with Rg and N_2 ligands. On the other hand, the M06-2X/aug-cc-pVTZ level has previously been shown to provide a reliable description of the interaction of Ar and N_2 ligands with the phenol and aminobenzonitrile cations in their ground electronic state.[21,27] Apparently, this level accounts well for the electrostatic, inductive, and dispersion forces present in such aromatic radical cations weakly interacting with nonpolar ligands. Moreover, spin contamination is negligible at the M06-2X level, with values of $\langle S^2\rangle - 0.75 = 0.023$ and 0.0003 before and after annihilation for t-AA^+ using the aug-cc-pVTZ basis. In general, all coordinates are relaxed during the search of stationary points on the potential energy surface without any symmetry restrictions. Vibrational analysis is used to establish the nature of the stationary points as minimum or transition state. Interaction energies (D_e) are corrected for harmonic zero-point energies (ZPE) to yield binding energies (D_0). Harmonic intramolecular frequencies are scaled by a factor of 0.9543 and 0.98 for frequencies above and below 2500 cm^{-1} to optimize the agreement between the calculated and the measured

frequencies of the N–H stretch and fingerprint modes of the AA^+ monomer. Such a dual scaling factor procedure accounts for the rather different anharmonicities of hydride stretch modes and skeletal vibrations in the fingerprint range.[56] Reported intermolecular frequencies are unscaled. The charge distribution is evaluated using the natural bond orbital (NBO) analysis.

3. Results and discussion

3.1 Quantum chemical calculations

Fig. 1 shows the minimum structures of *c*/*t*-AA^+ and the most stable *c*/*t*-AA^+–L dimer isomers with L = Ar and N_2. The corresponding structural, vibrational, and energetic data relevant for the present work are listed in Table 1. These include intramolecular parameters, such as the N–H and C═O bond lengths of the amide group (r_{NH}, r_{CO}), and the frequencies and IR intensities of the N–H and C═O stretch modes ($\nu_{NH/CO}$, $I_{NH/CO}$). Also listed are important parameters of the intermolecular bonds, such as bond lengths (R) and bond angles (θ_{NH-L}, θ_{H-NN}) as well as their dissociation energies ($D_{e/0}$). The notation of the cluster isomers employed in this work, *c*/*t*-$AA^{(+)}$–L_n(xH$y\pi$), indicates the number of H-bonded (x) and π-bonded (y) ligands L attached to *c*/*t*-$AA^{(+)}$, with $x + y = n$. IR stick spectra of *c*/*t*-AA^+ and their AA^+–L isomers with L = Ar and N_2 in the fingerprint and hydride stretch ranges are compared in Fig. 4. These cover the N–H and C–H stretch ranges ($\nu_{NH/CH}$), as well as the amide I (C═O stretch, ν_{CO}), amide II (in-plane N–H bend), and amide III (in-plane N–H bend coupled to C–N stretch) ranges characteristic for the –NH–CO– group. The corresponding geometric, vibrational, and energetic data for neutral *c*/*t*-AA and *c*/*t*-AA–L are also provided in Table 1.

3.1.1 AA and AA^+ monomers. In line with previous spectroscopic and quantum chemical data, the structure of neutral *t*-AA with C_s symmetry features a planar *N*-phenylamide unit in its ground electronic state (S_0). The N–H bond is rather short (r_{NH} = 1.0063 Å) leading to a relatively high frequency (ν_{NH} = 3482 cm^{-1}), in good agreement with experiment (3472 cm^{-1}).[44] On the other hand, the C═O bond is relatively weak (r_{CO} = 1.2103 Å) and associated with a low stretching frequency (ν_{CO} = 1773 cm^{-1}), again consistent with experiment (1728 cm^{-1}).[44] The calculated rotational constants of 3748, 788, and 654 MHz compare favourably with the measured values of 3675, 781, and 656 MHz, respectively.[47] In the neutral *c*-AA isomer, the phenyl plane is rotated by 35° with respect to the amide plane (dihedral C2–C1–N–H). It is calculated to be ΔE_0 = 757 cm^{-1} or ΔG_{298} = 954 cm^{-1} less stable than *t*-AA, somewhat higher than the recent rough experimental estimate of $\Delta G_{298} \sim 550$ cm^{-1}.[47] Its N–H and C═O bonds are longer than in *t*-AA by 3.3 and 1.8 mÅ, leading to frequency redshifts of $\Delta\nu_{NH} = -47$ cm^{-1} and $\Delta\nu_{CO} = -13$ cm^{-1} upon *trans* → *cis* isomerization. Thus, the two isomers can readily be distinguished by their IR spectra, although only the IR spectrum of *t*-AA has been measured yet.[44] The rotational barrier for *trans* → *cis* isomerization is calculated to be rather high ($V_b > 5000$ cm^{-1}).

The $^2A''$ ground electronic state of the planar *t*-AA^+ cation with C_s symmetry is obtained by removal of one electron from

Table 1 Selected geometrical parameters (Å, degree), vibrational frequencies (cm^{-1}), and dissociation energies (cm^{-1}) of AA, AA^+, and $AA^{(+)}$–L clusters (Fig. 1) calculated at the M06-2X/aug-cc-pVTZ level[a]

Species	r_{NH}	r_{CO}	ν_{NH}	ν_{CO}	D_e	D_0	R_{AA-L}[c]	θ_{NH-L}	θ_{H-NN}
t-AA	1.0063	1.2103	3482 (29)	1773 (258)					
c-AA	1.0096	1.2121	3435 (42)	1760 (561)					
t-AA–Ar(H)	1.0067	1.2105	3469 (67)	1774 (274)	305	220	2.6960	170.5	
t-AA–Ar(π)	1.0061	1.2106	3483 (29)	1772 (257)	478	325	3.3982		
c-AA–Ar(H)[b]	1.0098	1.2120	3440 (40)	1760 (536)	476	383	3.7305	65.3	
c-AA–Ar(π)	1.0097	1.2121	3434 (42)	1763 (572)	536	349	3.3913		
t-AA–N_2(H)	1.0069	1.2107	3456 (100)	1778 (279)	517	247	2.4265	172.8	176.2
t-AA–N_2(π)	1.0065	1.2102	3478 (29)	1774 (250)	667	449	3.1654		
c-AA–N_2(H)	1.0099	1.2134	3431 (75)	1756 (571)	537	281	2.5008	138.8	150.3
c-AA–N_2(π)	1.0097	1.2118	3427 (42)	1760 (570)	677	409	3.2602		
t-AA^+	1.0138	1.1890	3385 (101)	1869 (146)					
c-AA^+	1.0181	1.1903	3328 (126)	1850 (184)					
t-AA^+–He(H)	1.0137	1.1891	3403 (113)	1871 (148)	156	65	2.4120	167.3	
c-AA^+–He(H)	1.0180	1.1906	3338 (130)	1847 (183)	125	23	2.5628	123.3	
t-AA^+–Ar(H)	1.0156	1.1895	3340 (258)	1869 (156)	720	579	2.5018	178.3	
t-AA^+–Ar(π)	1.0137	1.1893	3382 (98)	1868 (142)	585	548	3.3191		
c-AA^+–Ar(H)	1.0200	1.1911	3296 (301)	1846 (173)	633	475	2.5002	178.7	
c-AA^+–Ar(π)	1.0180	1.1905	3351 (125)	1846 (180)	681	519	3.0723		
t-AA^+–Ar(CHp)	1.0138	1.1891	3385 (102)	1868 (145)	214	51	2.9116		
t-AA^+–Ar(CH_3)	1.0139	1.1892	3369 (100)	1867 (150)	225	140			
t-AA^+–N_2(H)	1.0168	1.1898	3324 (356)	1864 (157)	1227	977	2.2259	176.3	175.0
t-AA^+–N_2(π)	1.0136	1.1895	3387 (98)	1864 (143)	715	520	3.1486		
c-AA^+–N_2(H)	1.0215	1.1918	3278 (427)	1843 (180)	1186	907	2.1897	177.1	167.6
c-AA^+–N_2(π)	1.0179	1.1903	3351 (124)	1850 (184)	882	615	2.9308		

[a] IR intensities (km mol^{-1}) are listed in parentheses. The scaling factors are 0.9543 and 0.98 for frequencies above and below 2500 cm^{-1}. [b] Although the optimization started at a linear H-bonded configuration, the H-bond became strongly nonlinear for this isomer. [c] For π complexes, R gives the distance to the $AA^{(+)}$ plane.

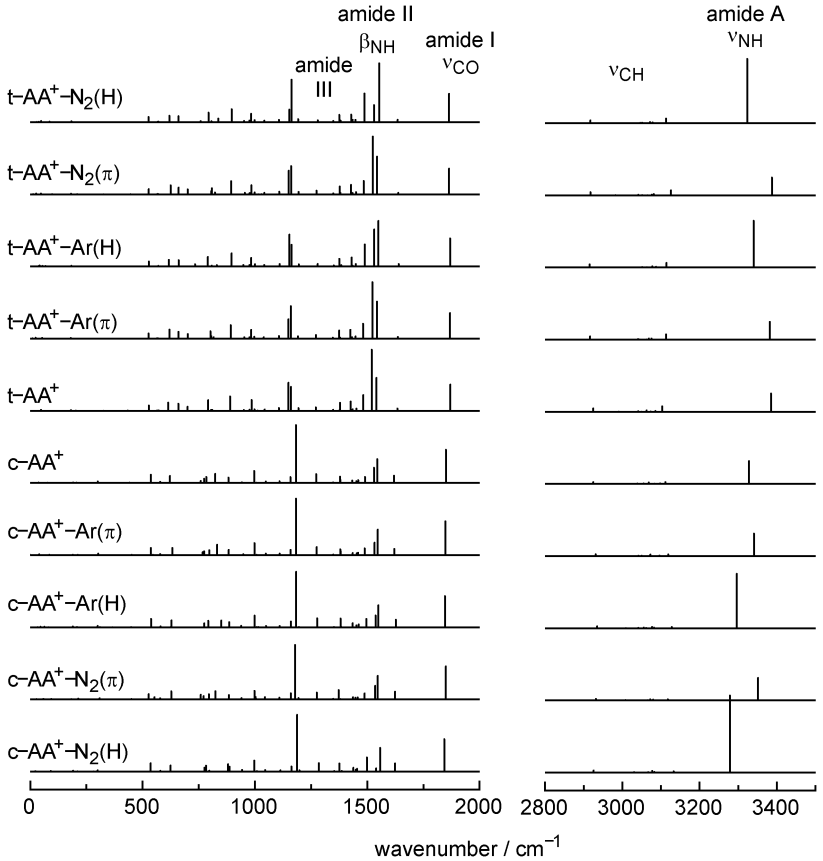

Fig. 4 IR stick spectra of *c*/*t*-AA$^+$ and *c*/*t*-AA$^+$–L dimer isomers (L = Ar/N$_2$) in the fingerprint and hydride stretch range obtained at the M06-2X/aug-cc-pVTZ level (Table 1 and Fig. 1).

the highest occupied molecular orbital. This bonding π(a″) orbital is delocalized over the aromatic ring and has also significant electron density on the amide group (Fig. S1 in ESI†). As a consequence, ionization of *t*-AA induces a remarkable elongation of the N–H bond (Δr_{NH} = +8 mÅ) and a drastic contraction of the C═O bond (Δr_{CO} = −21 mÅ). These structural changes translate directly into corresponding frequency shifts of $\Delta\nu_{NH}$ = −97 cm^{-1} and $\Delta\nu_{CO}$ = +96 cm^{-1}, respectively. The effects of ionization on other ring modes and amide modes of *t*-AA have been discussed in detail in the previous ZEKE study of *t*-AA$^+$.[46] In contrast to neutral *c*-AA, the *c*-AA$^+$ cation is also predicted to be planar (C_s) and about 1736 cm^{-1} (21.8 kJ mol^{-1}) less stable than *t*-AA$^+$. It can clearly be distinguished from the *t*-AA$^+$ cation by its very different geometrical and vibrational structure of the amide group (Fig. 4). For example, both the C═O and N–H bonds of *c*-AA$^+$ are slightly longer than in *t*-AA$^+$ by 1.3 and 4.3 mÅ, leading to lower ν_{CO} and ν_{NH} frequencies (by 19 and 57 cm^{-1}). These differences arise from different degrees of π-conjugation in both isomers, as indicated by the NBO charge distribution discussed below. The adiabatic ionization energies of *c*-AA and *t*-AA are calculated as IE = 66 656 and 65 677 cm^{-1}. The latter value agrees remarkably well with the measured value of 65 537 cm^{-1} available from the ZEKE spectra,[46] indicating that the chosen theoretical approach reliably describes the electronic structure of both the neutral and the cationic ground state of AA$^{(+)}$. Similarly, the calculated intramolecular frequencies of the amide torsion, amide in-plane bend and in-plane C–N stretch modes (48, 181, 890 cm^{-1}) of *t*-AA$^+$ compare favourably with those extracted from the ZEKE spectra (43, 181, 878 cm^{-1}).[46]

To investigate the potential energy surface for *cis–trans* isomerization, energies have been optimized for internal rotation around the amide HN–CO bond (Fig. 5). The amide

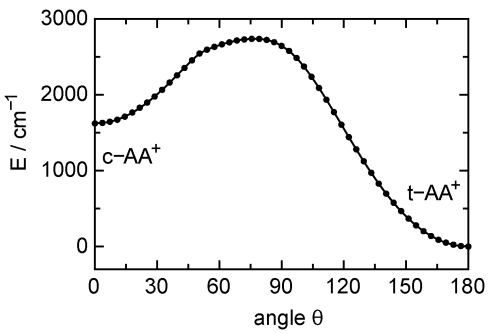

Fig. 5 Potential for *cis–trans* isomerization of AA$^+$ derived at the M06-2X/aug-cc-pVTZ level. All coordinates are relaxed for each amide dihedral angle θ (H–N–C–O), which varies between 180° (*t*-AA$^+$, E = 0) and 0° (*c*-AA$^+$, E = 1622 cm^{-1}) in steps of 3.6°. The barrier occurs at $\theta \sim 77°$ with V_b = 1116 cm^{-1} from *c*-AA$^+$.

dihedral angle θ (H–N–C–O) varies between 180° (*t*-AA$^+$) and 0° (*c*-AA$^+$) in steps of 3.6°. At this level, *c*-AA$^+$ is 1622 cm^{-1} less stable than *t*-AA$^+$, and *c*-AA$^+$ → *t*-AA$^+$ isomerization involves a significant barrier of V_b = 1116 cm^{-1} at $\theta \sim 77°$. As a consequence, if both isomers were produced in the supersonic plasma expansion they may easily be trapped and cooled down in their respective potential wells. As expected, the isomerization barrier in the open-shell cation ground state is much lower than for the closed-shell neutral molecule ($V_b > 5000$ cm^{-1}).

The NBO charge distributions of *t*-AA and *t*-AA$^+$ in their $S_0(^1A')$ and $D_0(^2A'')$ states are compared in Fig. 6. The excess charge upon removal of the bonding π(a″) electron, as determined by the charge difference of *t*-AA$^+$ and *t*-AA, is mainly localized on the aromatic phenyl ring (0.81 *e*) and the NH–CO amide group (0.14 *e*), whereas the CH_3 group remains mostly neutral (0.06 *e*). Thus, the aromatic ring as well as the highly positively charged proton of the amide group (0.42 *e*) will be the main attractive binding sites of *t*-AA$^+$ for neutral nonpolar ligands, leading to the formation of intermolecular π-bonds and H-bonds, respectively. The substantially different NBO charge distributions of *t*-AA$^+$ and *c*-AA$^+$ detailed in Fig. S2 in ESI† reveal that the phenyl ring in *c*-AA$^+$ carries less positive charge (0.75 *vs.* 0.81 *e*), whereas the amide group (0.20 *vs.* 0.14 *e*) and its N–H proton (0.43 *vs.* 0.42 *e*) are slightly more positive. Thus, the π-bonded ligands in *c*-AA$^+$–L(π) are shifted more toward the amide group than in *t*-AA$^+$–L(π) (Fig. 1), and also have slightly higher interaction energies D_e. On the other hand, the NH group is less acidic in *c*-AA$^+$–L(H), leading to slightly weaker H-bonds than in *t*-AA$^+$–L(H).

3.1.2 AA$^+$–L dimers. Several isomers have been identified on the *t*-AA$^+$–Ar potential. The planar H-bonded *t*-AA$^+$–Ar(H) dimer shown in Fig. 1 corresponds to the global minimum. Its nearly linear H-bond is characterized by a dissociation energy of D_0 = 579 cm^{-1}, an intermolecular separation of R = 2.50 Å, a bond angle of θ_{NHAr} = 178°, and intermolecular frequencies of β' = 38, β'' = 43, and σ = 69 cm^{-1}, respectively. The N–H donor bond elongates by Δr_{NH} = 1.8 mÅ upon formation of the H-bond with Ar, and as a result ν_{NH} exhibits a redshift of $\Delta\nu_{NH}$ = −45 cm^{-1} and an IR intensity enhancement of ΔI_{NH} = 155%. In addition, the N–H in-plane and out-of-plane bends at β_{NH} = 1540 and γ_{NH} = 700 cm^{-1} exhibit blueshifts of +9 and +33 cm^{-1} and also IR intensity changes upon H-bonding with Ar (183 → 253 and 22 → 13 km mol^{-1}). As expected, the properties of the C=O bond are nearly unaffected by H-bonding with Ar. As the corresponding H-bond in the *c*-AA$^+$–Ar(H) isomer is slightly weaker (D_0 = 475 cm^{-1}, R = 2.50 Å, θ_{NHAr} = 179°) than in *t*-AA$^+$–Ar(H), the impact on the N–H bond properties is correspondingly smaller (Δr_{NH} = 1.9 mÅ, $\Delta\nu_{NH}$ = −32 cm^{-1}, ΔI_{NH} = 139%). Similarly, β_{NH} = 1545 and γ_{NH} = 759 cm^{-1} exhibit smaller blueshifts of + 5 and + 24 cm^{-1}.

The π-bonded *t*-AA$^+$–Ar(π) local minimum shown in Fig. 1 is slightly less stable than the *t*-AA$^+$–Ar(H) global minimum, with D_0 = 548 cm^{-1}, an Ar-ring separation of R = 3.32 Å, and intermolecular frequencies of β_x = 10, β_y = 25, and σ_z = 54 cm^{-1}, respectively. The latter compare favourably with the values of β_x = 12 and β_y = 18 cm^{-1} measured by ZEKE spectroscopy.[50] Intermolecular π-stacking of Ar has essentially no effect on the geometric and vibrational properties of the N–H and C=O bonds, with $\Delta\nu_{NH/CO} < 3$ cm^{-1} and $\Delta I_{NH/CO} < 3$%. Similar arguments apply to the N–H bends β_{NH} and γ_{NH}. Isomerization between the π-bonded local minimum and the H-bonded global minimum involves significant barriers of $V_b(\pi \rightarrow H)$ = 195 cm^{-1} and $V_b(H \rightarrow \pi)$ = 226 cm^{-1}, suggesting that both isomers can readily be trapped in their respective minima once they are formed in the supersonic plasma expansion. Barriers of similar magnitude have previously been calculated for related Ar complexes with acidic aromatic cations.[14,25,27,57] The calculated IE shift upon Ar complexation, $\Delta IE = \Delta D_0$ = 548–325 = 223 cm^{-1} (ΔD_e = 107 cm^{-1}), corresponds to the increase in the binding energy of *t*-AA$^{(+)}$–Ar(π) upon ionization and is compatible with the value measured by ZEKE spectroscopy (142 cm^{-1}).[50] The binding energy in *c*-AA$^+$–Ar(π) is slightly weaker than in *t*-AA$^+$–Ar(π), D_0 = 519 *vs.* 548 cm^{-1}.

In addition to the global H-bound and local π-bound minima, further less stable local minima have been considered for *t*-AA$^+$–Ar, including those in which Ar binds in the molecular plane to either the CH_3 group or the aromatic CH bond in *para* position. Both structures with C_s symmetry have relatively low dissociation energies, $D_0(CH_3)$ = 140 cm^{-1} and D_0(CHp) = 51 cm^{-1} (Table 1), and are thus not considered in detail further. Although the potential energy surface of the *t*-AA$^+$–Ar dimer has been explored in some detail, there might be more local minima than those identified here. However, spectroscopically relevant for the current study are only the by far most stable H-bonded and π-bonded ones. Thus, the preferred cluster growth is predicted to start with the formation of the *t*-AA$^+$–Ar(H) bonded dimer core and then proceed via attachment of subsequent

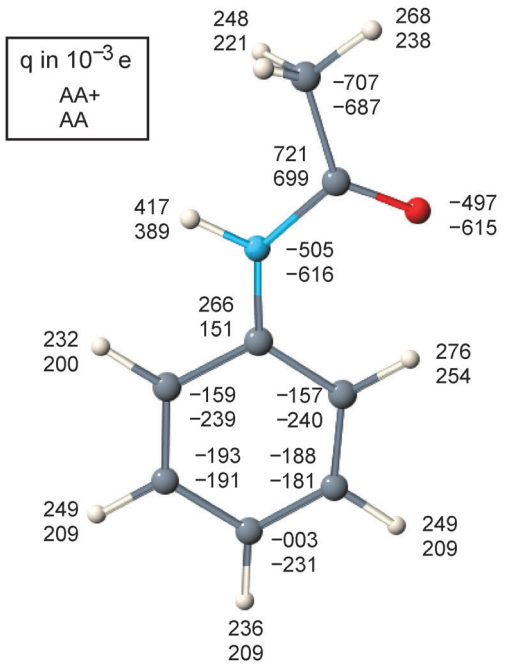

Fig. 6 NBO charge distribution (in 10^{-3} *e*) of *t*-AA (S_0, $^1A'$, bottom) and *t*-AA$^+$ (D_0, $^2A''$, top) in the ground electronic states evaluated at the M06-2X/aug-cc-pVTZ level.

ligands to the aromatic ring. The NBO analysis reveals only minor charge transfer from Ar to the *t*-AA^+ cation for any of the considered dimer isomers ($q_{Ar} < 0.015\ e$), in line with the view of mainly inductive and dispersive intermolecular attraction for H-bonding and π-stacking, respectively.

In general, the interaction of AA^+ with N_2 is stronger than with Ar due to its additional quadrupole moment and higher parallel polarizability.[9,58,59] As a result, complexation with N_2 has an enhanced impact on the intramolecular structural and vibrational properties as compared to Ar, in particular for the H-bonded isomer. The planar H-bonded *t*-AA^+–N_2(H) dimer corresponds to the most stable structure. The nearly linear H-bond is characterized by a binding energy of $D_0 = 977\ cm^{-1}$, an intermolecular separation of $R = 2.23$ Å, a bond angle of $\theta_{NHN} = 176°$, and intermolecular frequencies of $\beta' = 29$, $\beta'' = 38$, $\gamma' = 106$, $\gamma'' = 129$, and $\sigma = 88\ cm^{-1}$, respectively. The anisotropy of the charge-induced dipole and charge–quadrupole interaction favors a linear over a T-shaped approach of the N_2 ligand toward a positive charge.[9,27,58,60–67] The N–H donor bond stretches by 3 mÅ upon formation of the H-bond with N_2, leading to a redshift of $\Delta\nu_{NH} = -61\ cm^{-1}$ and $\Delta I_{NH} = 252\%$. The two N–H bends exhibit blueshifts of $\Delta\beta_{NH} = +13$ and $\Delta\gamma_{NH} = +58\ cm^{-1}$, while the properties of the C═O bond are again nearly unaffected. Due to the slightly weaker H-bond in *c*-AA^+–N_2(H), the monomer deformation upon complex formation is correspondingly smaller.

The π-bonded AA^+–N_2(π) local minima are substantially less stable than the corresponding H-bonded global minima. For example, the π-bond in *t*-AA^+–N_2(π) is characterized by $D_0 = 520\ cm^{-1}$, an N_2-ring separation of $R = 3.15$ Å, and intermolecular frequencies of $\beta_x = 13$, $\beta_y = 26$, $\gamma_x = 78$, $\gamma_y = 71$, and $\sigma_z = 56\ cm^{-1}$, respectively. The N_2 ligand points toward the C-atom in *ipso* position with respect to the amide group, because this atom carries the highest positive partial charge on the ring skeleton. Similar to Ar, π-bonding of N_2 has essentially no effect on the geometric and vibrational properties of the N–H and C═O bonds, with $\Delta\nu_{NH/CO} < 5\ cm^{-1}$. Interestingly, the N_2 ligand in *c*-AA^+–N_2(π) is more displaced toward the amide group leading to a slightly stronger interaction than in *t*-AA^+–N_2(π). The π-bonded AA^+–N_2(π) structures are only shallow local minima. Due to the much larger well depths at the H-bonded minima, the population of the π-bonded dimers in the supersonic plasma expansion is predicted to be small, and the cluster growth is expected to begin with H-bonding to the NH group for the first N_2 ligand followed by attachment to less stable (π-) binding sites. Similar to the Ar complexes, the NBO analysis reveals only minor charge transfer from N_2 to the AA^+ cation, with $q_{N2} < 0.02\ e$ for all structures.

3.2 Experimental IRPD spectra

3.2.1 Hydride stretch range. Fig. 7 compares the IRPD spectra of the AA^+–L dimers with L = He, Ar, and N_2 in the spectral range between 2800 and 3600 cm^{-1}. This spectral range covers mainly the N–H and C–H stretch fundamentals of AA^+ (amide I, ν_{NH}, ν_{CH}) and the assignment of the spectral features is guided by comparison with the linear IR absorption

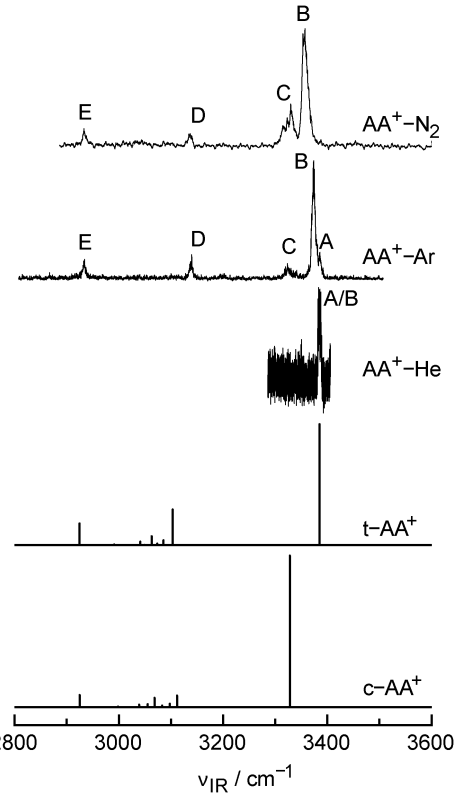

Fig. 7 IRPD spectra of AA^+–L dimers with L = He, Ar, and N_2 recorded in the C–H and N–H stretch range are compared to the linear IR absorption spectra calculated for *c*/*t*-AA^+ at the M06-2X/aug-cc-pVTZ level. The positions of the transitions for L = Ar and N_2 are listed in Table 2 along with their vibrational and isomer assignments.

spectra calculated for the *t*-AA^+ and *c*-AA^+ monomer isomers and their H-bonded AA^+–L(H) dimers. Corresponding IR spectra of larger AA^+–L_n clusters with L = He ($n \leq 2$), Ar ($n \leq 7$), and N_2 ($n \leq 10$) recorded in the dominant fragment channel are shown in Fig. S3 and S4 in ESI.† As ν_{NH} (amide A) is most sensitive to the cluster size, an enlarged view of the cluster spectra in this spectral range is offered in Fig. 8. The peak positions observed in the experimental spectra of AA^+–Ar/N_2 are listed in Table 2 along with the vibrational and isomer assignments.

The IRPD spectra of AA^+–He and AA^+–He_2 exhibit a single band (denoted A/B) in the N–H stretch range at 3385 and 3384 cm^{-1}, respectively, with a width of ~6 cm^{-1}. This transition can safely be assigned to the ν_{NH} fundamental of the *t*-AA^+–He_n clusters. As the interaction of AA^+ with He is very weak ($D_0 < 100\ cm^{-1}$), we cannot draw any reliable conclusion about the binding site of the He ligands (*e.g.*, H and/or π), as the shift will be insignificant at the current spectral resolution for any binding site (Table 1). Thus, the ν_{NH} band of AA^+–He at 3385 cm^{-1} is taken as close approximation of the free ν_{NH} fundamental of the *t*-AA^+ monomer and has been employed in Section 2 to derive the scaling factor for the high-frequency modes and serves as a reference point for the determination of the $\Delta\nu_{NH}$ frequency shifts upon complexation. Although ν_{NH} of *c*-AA^+ is predicted to be 25% stronger than ν_{NH} of *t*-AA^+, there is no sign of this isomer in the AA^+–He spectrum.

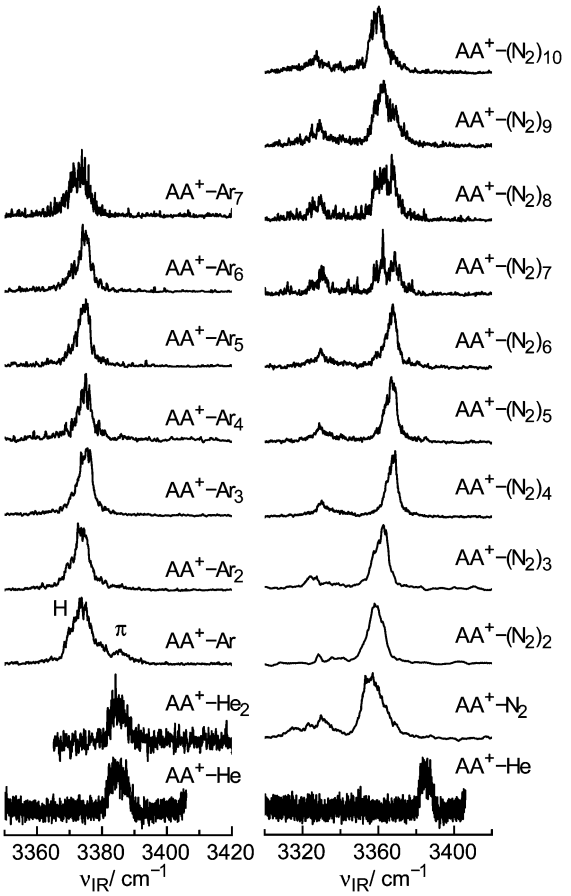

Fig. 8 Enlarged view of the IRPD spectra of $AA^+–L_n$ recorded in the dominant fragment channel in the vicinity of the N–H stretch fundamental.

The most intense feature in the IRPD spectrum of AA^+–Ar at 3373 cm^{-1} (band B) is redshifted by $\Delta\nu_{NH} = -12$ cm^{-1} from the corresponding AA^+–He transition, and is thus safely attributed to ν_{NH} of the H-bonded *t*-AA^+–Ar(H) dimer. The calculated shift, $\Delta\nu_{NH} = -45$ cm^{-1}, is somewhat larger than the experimental one, indicating that the computational approach overestimates the frequency shift. Another possibility is that the Fermi resonance interaction of ν_{NH} with vibrations assigned to band C may push the experimental ν_{NH} frequency to a higher value. The blueshaded band contour is typical for proton-donor stretch vibrations and thus supports the assignment to the H-bonded isomer. The observed redshift corresponds to the modest increase in H-bond energy upon ν_{NH} excitation. Assuming a calculated binding energy of $D_0 = 579$ cm^{-1}, the shift of $\Delta\nu_{NH} = -12$ cm^{-1} implies an increase in H-bond energy of only 2% upon ν_{NH} excitation. In addition, the AA^+–Ar spectrum also shows a weak transition at 3385 cm^{-1} (band A), which is essentially unshifted from ν_{NH} of AA^+–He and hence assigned to ν_{NH} of the π-bonded *t*-AA^+–Ar(π) dimer. For completeness, we note that the exact position of the Ar ligand in fact cannot be derived from the experimental spectrum in Fig. 8 alone. The only information derived from the vanishing frequency shift is that the Ar ligand is not occupying a H-bonded position. Comparison with related aromatic complexes[9] as well as the current computational studies reveals, however, that the π-binding site is by far the most stable non H-bonding site in this type of clusters and is thus the favoured assignment. Using the ratios of the integrated band intensities (~10) and the calculated IR oscillator strengths of ν_{NH} of the H-bonded and π-bonded isomers of *t*-AA^+–Ar (~2.6), their relative abundance in the plasma expansion can be estimated, and an upper limit of ~30% is derived for the population of the AA^+–Ar(π) isomer under the present experimental conditions. As previous studies demonstrated that the EI ion source predominantly produces the most stable isomer of a given cluster ion, this result clearly indicates that the H-bonded isomer is the global minimum, whereas the π-bonded dimer corresponds to a less stable local minimum. This conclusion is further supported by the IRPD spectra of the larger AA^+–Ar_n clusters and the quantum chemical calculations.

The most intense transitions in the IRPD spectra of AA^+–Ar_n with n = 2–7 occur within ±3 cm^{-1} from ν_{NH} of the H-bonded *t*-AA^+–Ar(H) dimer (band B). There are small but noticeable incremental blueshifts in the size range n = 1–5, which are followed by modest redshifts for n = 6–7. In addition, the bound ν_{NH} band exhibits enhanced splittings with increasing cluster size, indicating that the number of isomers increases with n. Although it is difficult to extract more definitive information about the sequential cluster growth from the IR spectral data, they confirm the rough picture that the first Ar ligand is H-bonded to the NH group whereas subsequent Ar ligands occupy less favourable binding sites such as π-stacking. Significantly, the AA^+–Ar_n spectra with $n \geq 2$ do not show any measurable signal in the range of ν_{NH} of free *t*-AA^+, indicating that the abundance of the *t*-AA^+–$Ar_n(n\pi)$ isomers is below the detection limit. This observation clearly confirms that the H-bond in *t*-AA^+–Ar_n clusters is more stable than any other binding site, including the π-bond.

In contrast to AA^+–Ar, the IRPD spectrum of AA^+–N_2 features only a single ν_{NH} band at 3355 cm^{-1} (band B), and its significant redshift of $\Delta\nu_{NH} = -30$ cm^{-1} upon N_2 complexation strongly suggests an assignment to the H-bonded *t*-AA^+–N_2(H) isomer, with a predicted shift of $\Delta\nu_{NH} = -61$ cm^{-1}, which similar to *t*-AA^+–Ar(H) is substantially larger than the measured one. The blueshaded band contour is more pronounced than for ν_{NH} of *t*-AA^+–Ar(H) due to the stronger H-bond with N_2 leading to a correspondingly larger $\Delta\nu_{NH}$ shift. There is essentially no signal in the spectral range of the free ν_{NH} mode of *t*-AA^+, indicating that the abundance of the less stable *t*-AA^+–$N_2(\pi)$ isomer is below the detection limit. From the achieved signal-to-noise ratio (~50) and the ratio of the predicted IR intensities (~3.6), we can estimate an upper limit for the *t*-AA^+–$N_2(\pi)$ population of 7%. This observation clearly confirms that the H-bond in (*t*-)AA^+–$(N_2)_n$ clusters is more stable than any other binding site.

The ν_{NH} bands of the larger AA^+–$(N_2)_n$ clusters with $n \geq 2$ shift in a similar fashion as those of AA^+–Ar_n, except that the incremental shifts and splittings due to isomers are more pronounced (Fig. 8). Incremental blueshifts of a few cm^{-1} from ν_{NH} of *t*-AA^+–N_2(H) in the size range n = 1–5 are again followed

Table 2 Band maxima observed in the IRPD spectra of AA^+–L (Fig. 7 and 10) compared to frequencies (in cm^{-1}) calculated at the M06-2X/aug-cc-pVTZ level and vibrational assignments[a]

	AA^+–Ar IRPD	AA^+–N_2 IRPD	*t*-AA^+ calc	*t*-AA^+–Ar(H) calc	*t*-AA^+–Ar(π) calc	*t*-AA^+–N_2(H) calc	*t*-AA^+–N_2(π) calc	Vibration[c]
A	3385		3385 (101)		3382 (98)		3387 (98)	ν_{NH} (π) (amide A)
B	3373	3355		3340 (258)		3324 (356)		ν_{NH} (H) (amide A)
C	3324/3319	3315						
D	3138	3137	3103 (30)	3114 (25)	3113 (29)	3113 (25)	3126 (27)	ν_{CHo}
E	2933	2933	2925 (18)	2915 (16)	2916 (17)	2917 (15)	2918 (17)	ν_{CH3} (sym)
F	1819	1818	1869 (146)	1869 (156)	1868 (142)	1864 (157)	1864 (143)	ν_{CO} (amide I)
G	1605		1634 (13)	1640 (14)	1636 (10)	1635 (14)	1638 (8)	ν_{CC} (ph, ν_{8a})
H	1538	1544	1540 (183)	1550 (253)	1543 (206)	1553 (326)	1544 (209)	ν_{CC} (ph, ν_{8b})/β_{NH} (amide II)
I	1527[b]	1533[b]	1520 (339)	1531 (206)	1523 (313)	1530 (95)	1524 (321)	β_{NH} (amide II)
K	1505	1519						
L	1487	1491	1482 (87)	1489 (122)	1481 (83)	1488 (159)	1484 (74)	ν_{CC} (ph, ν_{19a})/β_{NH} (amide II)
M	1452	1451	1452 (13)	1449 (14)	1448 (12)	1447 (14)	1450 (12)	β_{CH3} (asym)
N	1441							
O	1433	1434	1435 (8)	1435 (5)	1432 (8)	1435 (13)	1434 (8)	β_{CH3} (asym)
P	1424/1428	1424	1426 (52)	1431 (50)	1425 (49)	1428 (42)	1428 (52)	β_{CH} (ph, ν_{19b})
Q	1386	1386	1379 (44)	1376 (42)	1375 (45)	1375 (41)	1378 (43)	β_{CH3} (sym)
R	1355		1348 (6)	1351 (6)	1347 (5)	1349 (7)	1349 (6)	β_{CH} (ph, ν_3)
S	1284	1284	1271 (19)	1279 (14)	1272 (20)	1280 (11)	1274 (20)	β_{CH} (ph)/β_{NH} (amide III)
T	1203/1210		1194 (15)	1195 (12)	1191 (13)	1192 (17)	1194 (14)	β_{CH} (ph, ν_{9a})
U	1171/1160		1160 (133)	1163 (120)	1160 (180)	1163 (235)	1161 (156)	β_{CH} (ph, ν_{14})/ν_{CNC} (asym, am)
V	1149	1153	1149 (156)	1154 (177)	1149 (107)	1154 (70)	1151 (131)	ν_{CNC} (asym, am)/β_{CH} (ph, ν_{14})
W	1131							
X	994/983		985 (60)	983 (48)	983 (49)	983 (47)	984 (51)	ν_{CC} (am)
Y	878		890 (80)	896 (73)	893 (75)	897 (72)	894 (73)	ν_{CN} (am)/ν_{CC} (ph, ν_1)
Z	813		792 (59)	790 (53)	802 (41)	794 (53)	809 (34)	γ_{CH} (ph, ν_{11})

[a] IR intensities (in km mol^{-1}) are listed in parentheses. [b] Broad transition. [c] ν and β designate stretching and bending modes, respectively; am and ph designate modes localized mainly on the amide and phenyl groups, respectively; the numbering of the phenyl modes (ν_i) follows the Wilson notation for the benzene vibrations (ref. 71).

by smaller redshifts for n = 6–10. The ν_{NH} bands also display progressing splittings with increasing cluster size and also intensity variations of the individual subcomponents, indicating that there are several routes for cluster aggregation. Again, although it is difficult to extract more definitive information about the sequential cluster growth from the IR spectral data, they confirm the view that the first N_2 ligand is strongly H-bonded to the NH group and subsequent ligands form weaker bonds to the *t*-AA^+–N_2(H) dimer core. Significantly, the ν_{NH} shifts of the n = 2 cluster disfavour an assignment to a trimer structure, in which two N_2 ligands bind to the NH group resulting in a bifurcated double H-bond. Such structures were previously observed for N_2 clusters of the indole and tryptamine cations.[31,32] However, the calculations show that such a binding motif is less stable for *t*-AA^+–$(N_2)_2$.

The IRPD spectra of AA^+–L_n with L = He, Ar, and N_2 do not provide any evidence for the presence of cluster ions with *c*-AA^+. The ν_{NH} mode of *c*-AA^+ is predicted at 3328 cm^{-1} with high IR oscillator strength (126 km mol^{-1}). One might speculate that band C, which occurs in this frequency range in the spectra with L = Ar and N_2, may in fact arise from ν_{NH} of *c*-AA^+–L_n clusters. However, in marked contrast to ν_{NH} of *t*-AA^+–L_n, the position of band C does not depend much on the ligand L and the cluster size n. Thus, an assignment of band C to a Fermi resonance component of *t*-AA^+–L_n is clearly favoured over an assignment to ν_{NH} of *c*-AA^+–L_n (*vide infra*). The absence of any spectral signatures of *c*-AA^+–L_n is also consistent with the IRPD spectra recorded in the fingerprint range (Section 3.2.2).

In general, the frequency redshifts of proton donor stretch vibrations in H-bonded AH^+–L dimers are correlated with the proton affinity (PA) of the ligand L.[9,15,60,61,68,69] Fig. 9 shows the measured and calculated ν_{NH} frequencies of *t*-AA^+–L(H) dimers as a function of the PA of L for L = He, Ar, N_2, and H_2O,[70] which shows a monotonic dependence. Comparison of AH^+–L dimers for a variety of aromatic molecules A reveals that the acidity of the NH group in aromatic amide radical cations is rather weak. For example, the (averaged) $\Delta\nu_{NH}$ redshifts for NH–Ar complexation are −12 cm^{-1} for AH^+ = aniline$^+$,[25] −15 cm^{-1} for 4-cyanoaniline$^+$,[27] −29 cm^{-1} for indole$^+$,[31] and −69 cm^{-1} for imidazole.[29] Thus, the measured shift for AH^+ = *t*-AA^+ of

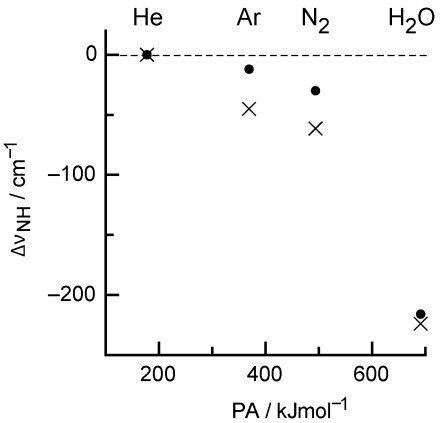

Fig. 9 Experimental complexation-induced redshifts $\Delta\nu_{NH}$ of H-bonded AA^+–L(H) dimers (filled circles) as a function of the proton affinity (PA) of the ligand L for L = He, Ar, N_2, and H_2O (178, 369, 494, and 691 kJ mol^{-1}),[70] compared to shifts for *t*-AA^+–L(H) calculated at the M06-2X/aug-cc-pVTZ level (crosses).

−12 cm^{-1} is rather small and comparable to aniline cations. Despite its weak proton donor ability, the H-bonded *t*-AA^+–Ar(H) dimer is still more stable than the π-bond in *t*-AA^+–Ar(π), indicating that the preference for H-bonding over π-stacking in Ar complexes of acidic aromatic cations holds even for low acidity.

In addition to ν_{NH} (bands A and B), the IRPD spectra of AA^+–L_n with L = Ar and N_2 in Fig. 7 and Fig. S3 and S4 in ESI† reveal three less intense transitions (denoted C–E) in the 2800–3600 cm^{-1} range. Band E occurs between 2932 and 2936 cm^{-1} for all AA^+–L_n clusters considered and can readily be assigned to the symmetric C–H stretch mode of the CH_3 group of *t*-AA^+ in *t*-AA^+–L_n (ν_{CH3}) by comparison with the spectrum calculated for the *t*-AA^+ monomer (ν_{CH3} = 2925 cm^{-1}). This mode is the lowest C–H stretch frequency and has a significant IR intensity (18 km mol^{-1}). The fact that there is little variation in frequency and IR intensity as a function of L and *n* suggests that the CH_3 group does not belong to the favourable ligand binding sites of *t*-AA^+. Band D of all AA^+–L_n clusters is observed between 3136 and 3142 cm^{-1} and can readily be attributed to the isolated aromatic C–H stretch of the *ortho* CH group of the phenyl ring (ν_{CHo}) in *trans* position of the NH group, which has a calculated frequency of ν_{CHo} = 3103 cm^{-1} for *t*-AA^+ and appreciable IR activity (30 km mol^{-1}). All other aromatic and aliphatic C–H stretch fundamentals of the CH_3 and C_6H_5 groups in *t*-AA^+ are predicted between ν_{CH3} = 2925 and ν_{CHo} = 3103 cm^{-1} but their IR oscillator strength appears to be too low (<8 km mol^{-1}) to be detected in the IRPD spectra of AA^+–L_n. Clearly, the appearance of the IRPD spectra of AA^+–L_n in the C–H stretch range is compatible with clusters of only the *t*-AA^+ isomer (*e.g.*, intense ν_{CHo} and ν_{CH3} transitions), and no sign of the presence of *c*-AA^+–L_n clusters is visible.

In addition to ν_{NH} (A/B) and ν_{CH} fundamentals (D/E), the IRPD spectra of AA^+–L_n show several absorptions in the frequency range 3320–3340 cm^{-1} summarized as band C. These transitions are outside of the range of the C–H stretch fundamentals (ν_{CH} = 2900–3150 cm^{-1}). In addition, their IR activity seems to be strongest for those AA^+–L_n clusters with the lowest ν_{NH} frequency, *e.g.* for *t*-AA^+–N_2(H). Hence, they are attributed to overtone and/or combination bands, which gain their oscillator strength *via* anharmonic coupling (Fermi resonance) with the strongly IR active ν_{NH} fundamental. At present, it is unclear whether the various components of band C arise from several vibrational modes or just from a single vibrational mode of the various isomers of a single AA^+–L_n cluster size. The IR spectrum of neutral *t*-AA also shows a Fermi doublet in the N–H stretch range at 3440 and 3472 cm^{-1} and the first component was assigned to the first overtone of the C═O stretch, $2\nu_{CO}$.[44] However, the ν_{CO} fundamentals of the *t*-AA^+–L_n clusters are observed near 1820 cm^{-1}, *i.e.* the $2\nu_{CO}$ overtone cannot account for the Fermi multiplets near 3330 cm^{-1}. In contrast, the only other first overtone of *t*-AA^+ calculated in the required frequency range is that of the symmetric aromatic C–C stretch mode $2\nu_{8a}$ predicted at 3282 cm^{-1}. However, this mode shows little coupling with the N–H stretch and has little IR activity (13 km mol^{-1}). As a more realistic and currently favoured alternative, band C may be produced by combination bands of the very IR active ν_{CO} fundamental (amide I) with other strongly IR active modes near ~1530 cm^{-1}, which all feature strong N–H bend character (amide II) and thus can readily couple to the N–H stretch (amide A).

At this stage, it is noted that the IRPD spectra of larger *t*-AA^+–$(N_2)_n$ clusters display additional features (X–Z in Fig. S3 and S4 in ESI†), which increase in intensity as a function of *n*. At present, it is unclear whether these transitions indeed arise from *t*-AA^+–$(N_2)_n$ or whether they are resonances of isobaric X^+–$(N_2)_p$ clusters with unknown X and *p*. Such contaminations are possible despite the tandem mass spectrometric approach.[24]

Comparison of the IR spectra of *t*-AA^+–Ar and *t*-AA[44] in Fig. S5 in ESI† reveals the spectroscopic effects of ionization on the properties of the N–H and C–H bonds as discussed in Section 3.1. The calculations predict a redshift of $\Delta\nu_{NH}$ = −97 cm^{-1}, which is consistent with the measured value of −87 cm^{-1}. The N–H bond in *t*-AA^+ becomes much weaker and more acidic in the cation ground state. On the other hand, all aromatic C–H stretch frequencies are predicted to increase upon ionization (by 9–25 cm^{-1}), and indeed the ν_{CHo} frequency measured for *t*-AA^+–L_n (3139 ± 3 cm^{-1}) is larger than that for *t*-AA (3098 cm^{-1}). The predicted aliphatic C–H stretch frequencies of the methyl group in *t*-AA^+ are almost not affected upon ionization, and again this trend is confirmed by the small observed redshift of $\Delta\nu_{CH3}$ = −8 cm^{-1}.

3.2.2 Fingerprint range. Fig. 10 compares the IRPD spectra of the AA^+–L dimers with L = Ar and N_2 in the fingerprint range

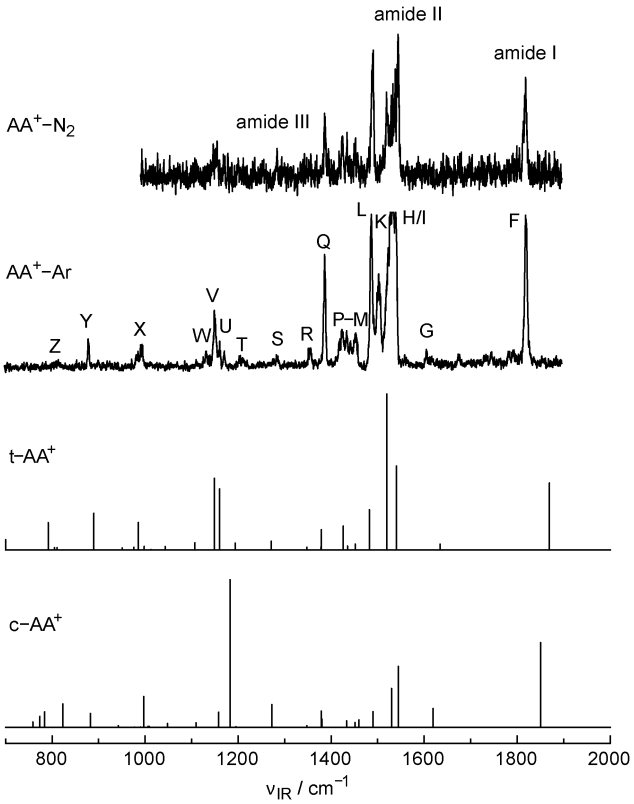

Fig. 10 IRPD spectra of AA^+–L dimers with L = Ar and N_2 recorded in the fingerprint range are compared to the linear IR absorption spectra for *c*/*t*-AA^+ calculated at the M06-2X/aug-cc-pVTZ level. The positions of the transitions are listed in Table 2 along with their vibrational and isomer assignments. The bands near 1530 cm^{-1} in the AA^+–Ar spectrum are saturated (an unsaturated spectrum is available in Fig. S6 in ESI†).

between 700 and 1900 cm^{-1}. Corresponding IR spectra of larger AA^+–L_n clusters with L = Ar ($n \leq 4$) and N_2 ($n \leq 3$) recorded in the dominant fragment channels are shown in Fig. S6 and S7 in ESI.† The peak positions observed in the experimental spectra for $n = 1$ are listed in Table 2 along with their vibrational and isomer assignments. The strong bands in the AA^+–Ar spectrum in Fig. 10 are saturated as this spectrum has been recorded with high detector sensitivity in order to detect the weak transitions. An unsaturated spectrum is provided in Fig. S6 in ESI.† A comparison between the IRPD spectrum of AA^+–Ar with the IR spectrum of neutral *t*-AA is given in Fig. S8 in ESI.† The fingerprint range covers mainly the amide I–III bands of the amide group including its C=O stretch and N–H bend fundamentals (ν_{CO}, β_{NH}) as well as C–H bend and rock vibrations of the aromatic ring skeleton and the CH_3 group. The assignment of the spectral features is again guided by comparison with the linear IR absorption spectra calculated for the *t*-AA^+ and *c*-AA^+ monomer isomers (Fig. 10) and the H-bonded AA^+–L(H) dimers (Fig. 4). In general, the coarse structure of all AA^+–L_n spectra is very similar in the fingerprint range, and the major variations are found in the amide II region near 1500 cm^{-1} (Fig. S9 in ESI†). From the comparison of the spectra in Fig. 10, it is again immediately obvious that only dimers with *t*-AA^+ contribute to the measured AA^+–L spectra. For example, spectra calculated for *c*-AA^+(–L) predict the strongest transition near 1200 cm^{-1} (amide III band, ν_{CN} stretch), while the experimental spectra display their most intense bands near 1500 cm^{-1}, in good agreement with the spectra calculated for *t*-AA^+(–L).

The single intense and quite isolated transition at 1818 cm^{-1} (band F) in the amide I region of the AA^+–L_n clusters does not show any significant dependence on the ligand L and the cluster size and can safely be assigned to the ν_{CO} fundamental of the *t*-AA^+ rotamer. The somewhat higher frequency calculated for *t*-AA^+ (1869 cm^{-1}) implies that the harmonic approach at the M06-2X/aug-cc-pVTZ level using a scaling factor of 0.98 overestimates the measured fundamental frequency by about 51 cm^{-1}. In the case of neutral *t*-AA, this theoretical approach overestimates ν_{CO} by a similar amount of 45 cm^{-1}, indicating that this level might have some problems in describing the C=O bond properties. Ionization of *t*-AA strengthens the C=O bond, and the resulting observed frequency increase of $\Delta\nu_{CO}$ = +90 cm^{-1} is compatible with the predicted change of +96 cm^{-1}. The ν_{CO} frequency of *c*-AA^+ is predicted to be significantly lower than that of *t*-AA^+ (by 19 cm^{-1}). As no second intense transition is detected in the ν_{CO} range in the IRPD spectra of AA^+–L_n, this result provides further evidence that these spectra are largely dominated by clusters of the *t*-AA^+ cation, a conclusion already suggested from the analysis of the spectra measured in the hydride stretch range.

Inspection of the amide II range reveals strong transitions (bands L, H, I) between 1480 and 1550 cm^{-1} assigned to modes involving strong N–H in-plane bend contributions more or less coupled to C–C stretch modes of the phenyl ring. These transitions dominate the fingerprint range, and their positions and intensities are well reproduced by the calculations. These amide II modes are also the transitions in the fingerprint range that are most sensitive to the type and number of ligands (Fig. S9 in ESI†), with shifts of up to 10 cm^{-1} for the cluster sizes investigated. The two weak transitions M and O as well as the strong band Q arise from asymmetric and symmetric C–H bends of the methyl group. In contrast to neutral *t*-AA, the intensity of the amide III transition (band S) is quite weak in the IR spectra of *t*-AA^+–L_n. There are a number of modes of the phenyl ring, for which we adopt the notation of Wilson.[71] These include the in-plane C–H bends ν_{19b} (P), ν_3 (R), and $\nu_{9a/14}$ (T/U), the out-of-plane C–H bend ν_{11} (Z), and the symmetric ring C–C stretch ν_1 which is strongly coupled to the amide C–N stretch (Y). Further bands of the amide group include the C–C stretch (X) and the asymmetric C–N–C stretch (V). In general, all intense bands predicted by the calculations for *t*-AA^+ are observed in the IRPD spectrum of AA^+–Ar and agree well with respect to their frequencies and relative IR intensities, supporting the vibrational and isomer assignment. Apart from the lower signal-to-noise ratio, the IRPD spectra of AA^+–$(N_2)_n$ are quite similar to those of AA^+–Ar_n. The comparison of the IR spectra of *t*-AA^+–Ar and neutral *t*-AA–Ar in Fig. S8 in ESI† illustrates the drastic changes in the geometric and vibrational structure of *t*-AA induced by ionization for the phenyl, amide, and methyl groups. These changes are well reproduced by the calculations.

3.3 Photofragmentation branching ratios and binding energies

In this section, we derive experimental binding energies (D_0) from observed photofragmentation branching ratios and compare these to calculated values listed in Table 1 ($D_{e/0}$). We consider both theoretical values ($D_{e/0}$) because the computational M06-2X approach substantially overestimates the contribution of ZPE arising from the highly anharmonic intermolecular modes.[21]

Table 3 summarizes the photofragmentation branching ratios observed in the IRPD process of AA^+–L_n clusters described in eqn (1) using the ν_{NH} resonance of the most stable isomer of a given cluster size. In agreement with previous observations for related systems, all AA^+–L_n cluster sizes investigated exhibit a

Table 3 Photofragmentation branching ratios (in %) of AA^+–L_n complexes for the photoinduced reaction in eqn (1) measured for the ν_{NH} fundamental[a]

L	*n*	*m* = 0	*m* = 1	*m* = 2	*m* = 3	*m* = 4	*m* = 5	ν_{NH}
He	1–2	100						3385
Ar	1–4	100						3374
	5	70	30					3374
	6		100					3374
	3		100					1527[b]
N_2	1–3	100						3367
	4	30	70					3367
	5	5	85	10				3367
	6		5	95				3367
	7			55	45			3367
	8				65	35		3356
	9					80	20	3356
	10						100	3356

[a] Only channels contributing more than 5% are listed. Uncertainties are estimated as 5%. [b] Measured at resonances in the fingerprint range.

rather narrow range of fragment channels (m) upon LID of a parent cluster (n), and this information can be used to extract ligand binding energies within the framework of a simple model. This model relies on the following rough approximations. (i) The difference in the internal energies of the parent cluster and the fragmentation products as well as the kinetic energy release is neglected. (ii) Only single ligands are evaporated, and those with smaller binding energies are evaporated first. (iii) Three-body forces are assumed to be small. (iv) The whole absorbed photon energy under the current single-photon absorption conditions ($\nu_{NH} \sim 3355$–3385 cm^{-1}) is available for ligand evaporation. (v) Ligands at similar binding sites are assumed to have the same binding energy, which are classified as D_0(H) and $D_0(\pi)$. Moreover, we infer from the IRPD spectra that $D_0(H) \geq D_0(\pi)$ for L = Ar and $D_0(H) \gg D_0(\pi)$ for L = N_2. Additional information comes from the IRPD spectra in the fingerprint range recorded in different fragment channels, which allow for extracting further thresholds for dissociation energies. For example, Fig. 11 shows the IRPD spectra of AA$^+$–Ar$_2$ recorded in the AA$^+$ and AA$^+$–Ar fragment channel, indicated as n–m = 2–0 and 2–1, respectively. The vibrations of AA$^+$–Ar$_2$ with frequencies below 1385 cm^{-1} occur only in the 2–1 fragment channel (loss of one Ar ligand), while those above 1150 cm^{-1} are only detected in the 2–0 channel (loss of two Ar ligands). From these thresholds, we can infer that the total binding energy of the two Ar ligands in AA$^+$–Ar$_2$, $D_0(H) + D_0(\pi)$, lies in the interval 1150–1385 cm^{-1}.

Analysis of all available photofragmentation data of L = Ar yields rough estimates of $D_0(\pi) < 700$ cm^{-1} and $570 < D_0(H)/\text{cm}^{-1} < 880$, *i.e.* $D_0(H) = 730 \pm 160$ cm^{-1}, with the additional restriction $D_0(H) > D_0(\pi)$. Using the assumption $D_0(H) \sim D_0(\pi)$, as suggested from the calculations, we obtain $570 < D_0(H/\pi)/\text{cm}^{-1} < 700$, in agreement with the calculated values of $D_{e/0}(\pi) = 585/548$ cm^{-1} and $D_{e/0}(H) = 720/579$ cm^{-1}, respectively. This match provides further evidence that the M06-2X/aug-cc-pVTZ level provides a reliable prediction of the AA$^+$–Ar interaction in both the H-bonded and π-bonded parts of the potential. Initial calculations at the lower M06-2X/6-311+G** level resulted in the reversed order $D_{e/0}(\pi) = 588/595$ cm^{-1} > $543/400$ cm^{-1} = $D_{e/0}$(H), which is not compatible with experiment for both the D_e and D_0 values.

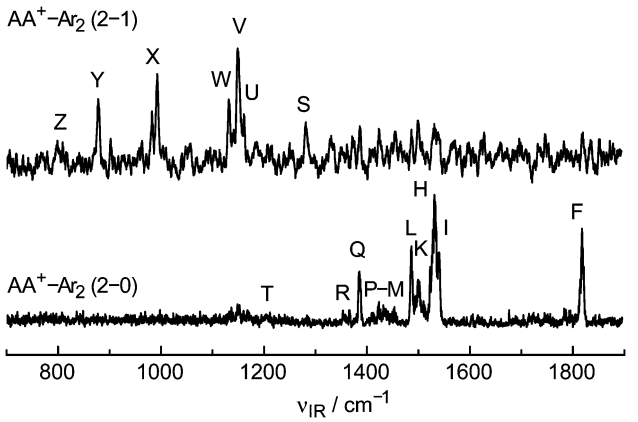

Fig. 11 IRPD spectra of AA$^+$–Ar$_2$ recorded in the AA$^+$ (bottom) and AA$^+$–Ar (top) fragment channel, indicted as n–m = 2–0 and 2–1, respectively. The positions of the transitions for AA$^+$–Ar are listed in Table 2 along with their vibrational and isomer assignments. The vibrations of AA$^+$–Ar$_2$ with frequencies below 1300 cm^{-1} occur in the 2–1 fragment channel (loss of one Ar ligand), while those above 1300 cm^{-1} are detected in the 2–0 channel (loss of two Ar ligands).

For neutral t-AA–Ar, the binding energies for the two considered isomers are calculated as $D_0(\pi) = 325$ cm^{-1} and $D_0(H) = 220$ cm^{-1}, *i.e.*, in the S_0 state the π-bond is clearly more stable than the H-bond. All spectroscopic data are consistent with a π-bonded t-AA–Ar(π) global minimum in S_0,[50] and no evidence for a less stable H-bonded local minimum was reported. While the attraction in t-AA–Ar(π) is dominated by dispersion forces between Ar and the highly polarizable π electrons of the aromatic ring, ionization increases its binding energy due to additional charge-induced polarization forces. The calculated increase in binding energy upon ionization, $\Delta D_0(\pi) = 223$ cm^{-1}, is compatible with the value of 142 cm^{-1} extracted from the ZEKE spectra.[50] The H-bond in neutral t-AA–Ar(H) is predicted to be weak in S_0, $D_0(H) = 220$ cm^{-1}, but gains substantial stabilization upon ionization, $\Delta D_0(H) = 359$ cm^{-1}, due to strong charge-induced dipole forces arising from the large positive partial charge on the N–H proton. Hence, clearly ionization induces a π → H switch in the preferred ion–ligand binding motif of t-AA$^{(+)}$–Ar.

Analysis of the photofragmentation data of L = N_2 yields $D_0(H) = 1150 \pm 50$ cm^{-1} and $D_0(\pi) = 725 \pm 25$ cm^{-1}, consistent with the calculated values of $D_{e/0}(H) = 1227/977$ cm^{-1} and $D_{e/0}(\pi) = 715/520$ cm^{-1}. The corresponding calculated values for neutral t-AA$^+$–N_2 are $D_0(H) = 247$ cm^{-1} and $D_0(\pi) = 449$ cm^{-1}. Hence, similar to t-AA–Ar, the calculations predict an ionization-induced π → H switch in the most stable ion–ligand binding motif also for AA$^{(+)}$–N_2. So far, no spectroscopic or quantum chemical data have been available for neutral AA–N_2.

3.4 Implications for ionization-induced isomerization

IR spectroscopy and quantum chemical calculations presented here convincingly demonstrate the ionization-induced π → H switch in the preferred binding motif for t-AA$^{(+)}$–Ar. The ZEKE spectra of t-AA$^+$–Ar generated by isomer-selective REMPI of the neutral π-bonded complex have been interpreted with a π-bonded cation isomer, consistent with vertical Franck–Condon factors.[50] These threshold ionization spectra do not exhibit any signature of the more stable H-bonded complex, probably due to the modest excess energy used for the ionization step achieved by two-colour two-photon (1 + 1′) REMPI. In contrast, IR spectra of the t-AA$^+$–Ar$_n$ clusters (n = 1–2) produced by one-colour two-photon (1 + 1) REMPI of π-bonded t-AA–Ar$_n$ show the signatures of the H-bonded dimer.[40] These REMPI-IR spectra are compared to the current EI-IR spectra in Fig. S10 in ESI.† The REMPI-IR spectra display a systematic redshift of ~7 cm^{-1} compared to the EI-IR spectra which probably arises from calibration issues in the REMPI-IR study. The accuracy of the calibration of the EI-IR spectra to better than 1 cm^{-1} is assured by a wavemeter monitored simultaneously with the IR laser scan. The REMPI-IR spectrum of t-AA$^+$–Ar shows two peaks in the N–H stretch range with similar intensity and separated by ~10 cm^{-1}.[40]

In the previous work, this splitting could not be explained. Here, we propose that the two bands arise from the ν_{NH} transitions of t-AA^+–Ar(π) and t-AA^+–Ar(H), respectively, which are split by $\sim$12 cm^{-1} in the corresponding EI-IR spectra. The significant intensity of the t-AA^+–Ar(H) isomer in the REMPI-IR spectrum indicates that after the REMPI process a substantial population of the initially π-bonded isomer has been converted into the H-bonded configuration, probably due to the large excess energy available from 1 + 1 REMPI, which enables at least part of the population to overcome the $\pi \rightarrow$ H isomerization barrier. A similar finite π/H population equilibrium has recently been observed in the REMPI-IR spectra of phenol$^+$–Rg dimers (Rg = Ar and Kr).[17,19,37–39] Interestingly, Ar dimers of aminobenzonitrile did not show any $\pi \rightarrow$ H isomerization yield.[27,28]

The REMPI-IR spectra of the π-bonded t-AA^+–$Ar_2(2\pi)$ trimer show mainly the ν_{NH} band of the t-AA^+–$Ar_2(H\pi)$ isomer, indicating nearly unity yield for the $\pi \rightarrow$ H isomerization of one of the Ar ligands.[33,37,39] Again, this result is similar to that observed previously for the phenol$^+$–Ar_2 trimer, for which the isomerization timescale has been measured in real time as $\sim$7 ps.[33,37] The 100% yield for $\pi \rightarrow$ H isomerization in complexes with two Ar ligands has been explained by fast intracluster vibrational energy redistribution enabled by the presence of the second Ar ligand.

No spectroscopic information is available for neutral AA–$(N_2)_n$ complexes. However, comparison with the related aniline–N_2 complex[72] strongly suggests that AA–N_2 dimers have a π-bonded equilibrium structure in the S_0 state, in line with the present quantum chemical calculations (Table 1). Thus, also the AA–N_2 cluster is expected to show the ionization-induced $\pi \rightarrow$ H site switching in the preferred ligand binding motif.

4. Concluding remarks

Size-selected AA^+–L_n complexes with L = Ar and N_2 have been characterized by IR spectroscopy and quantum chemical calculations to characterize the intermolecular potential of this prototypical aromatic amide cation with a nonpolar and quadrupolar solvent. The data provide a first impression of the microsolvation of an aromatic amide with a hydrophobic environment. Systematic shifts observed in the N–H stretch frequencies ν_{NH} (amide A band) as a function of the type and degree of solvation as well as the analysis of the photofragmentation data provide a quantitative picture of the interaction strengths and the cluster growth sequence, which are fully consistent with the calculations. For both ligands, H-bonding to the amide NH group is found to be more stable than π-stacking to the aromatic ring. However, the acidity of the NH group is relatively small. The preferred cluster growth begins with H-bonding of the ligands to the NH group and further ligands are attached to the phenyl ring and other less favourable binding sites. This is in contrast to solvation with hydrophilic solvents like water. AA^+–$(H_2O)_n$ clusters form structures, in which a H-bonded solvent network is strongly H-bonded to the NH group.[34,40,73] Comparison of the IRPD spectra of AA^+–L_n with calculated spectra demonstrates that the experimental spectra are dominated by clusters composed of the t-AA^+ rotamer and no indication for the presence of the less stable c-AA^+ is obtained. The IRPD spectra of AA^+–L_n recorded in the hydride stretch and fingerprint ranges provide for the first time valuable experimental information about the geometric and vibrational properties of t-AA^+ in the important amide A and I–III ranges. In particular, comparison with the corresponding neutral t-AA species reveals the effects of ionization on structure and bonding. Removal of an electron from the bonding π orbital (HOMO), which is largely delocalized over both the phenyl and amide moieties, strengthens the C=O bond and weakens the N–H bond of the amide. Significantly, ionization changes the preferred ion–solvent recognition motif in AA^+–Ar/N_2 from π-bonding in the neutral to H-bonding in the cation electronic ground state. This $\pi \rightarrow$ H change upon ionization was not detected in previous photoionization spectra of t-$AA^{(+)}$–Ar,[50] which do not detect the most stable H-bound global minimum in the cation due to restrictions from the Franck–Condon principle. Future efforts will concentrate on time-resolved spectroscopic measurements to probe the dynamics of the $\pi \rightarrow$ H site-switching reaction in AA^+–L_n with L = Ar and N_2 in real time, using picosecond pump–probe spectroscopy.[34,36]

Acknowledgements

This study was supported by DFG (DO 729/4-2), MEXT (Innovative Areas 2503 Japan), and the Core-to-Core Program of JSPS. Matthias Schmies is grateful for an Elsa Neumann fellowship.

References

1 E. A. Meyer, R. K. Castellano and F. Diederich, *Angew. Chem., Int. Ed.*, 2003, **42**, 1210.
2 L. M. Salonen, M. Ellermann and F. Diederich, *Angew. Chem., Int. Ed.*, 2011, **50**, 4808.
3 J. P. Schermann, *Spectroscopy and Modelling of Biomolecular Building Blocks*, Elsevier, Amsterdam, 2008.
4 P. Hobza and K. Müller-Dethlefs, *Non-covalent interactions*, The Royal Society of Chemistry, Cambridge, 2010.
5 K. Müller-Dethlefs and P. Hobza, *Chem. Rev.*, 2000, **100**, 143.
6 K. Müller-Dethlefs, O. Dopfer and T. G. Wright, *Chem. Rev.*, 1994, **94**, 1845.
7 B. Brutschy, *Chem. Rev.*, 2000, **100**, 3891.
8 K. S. Kim, P. Tarakeshwar and J. Y. Lee, *Chem. Rev.*, 2000, **100**, 4145.
9 O. Dopfer, *Z. Phys. Chem.*, 2005, **219**, 125.
10 J. E. Braun, T. Mehnert and H. J. Neusser, *Int. J. Mass Spectrom.*, 2000, **203**, 1.
11 H. J. Neusser and K. Siglow, *Chem. Rev.*, 2000, **100**, 3921.
12 G. L. Perlovich, T. V. Volkova and A. Bauer-Brandl, *J. Pharm. Sci.*, 2006, **95**, 2158.
13 N. Solcà and O. Dopfer, *Chem. Phys. Lett.*, 2000, **325**, 354.
14 N. Solcà and O. Dopfer, *J. Mol. Struct.*, 2001, **563/564**, 241.
15 N. Solcà and O. Dopfer, *J. Phys. Chem. A*, 2001, **105**, 5637.
16 N. Solcà and O. Dopfer, *Chem. Phys. Lett.*, 2003, **369**, 68.

17 A. Takeda, H. S. Andrei, M. Miyazaki, S. I. Ishiuchi, M. Sakai, M. Fujii and O. Dopfer, *Chem. Phys. Lett.*, 2007, **443**, 227.
18 A. Patzer, J. Langer, H. Knorke, H. Neitsch, O. Dopfer, M. Miyazaki, K. Hattori, A. Takeda, S. I. Ishiuchi and M. Fujii, *Chem. Phys. Lett.*, 2009, **474**, 7.
19 M. Miyazaki, S. Tanaka, S. Ishiuchi, O. Dopfer and M. Fujii, *Chem. Phys. Lett.*, 2011, **513**, 208.
20 A. Armentano, M. Riese, M. Taherkhani, M. B. Yezzar, K. Müller-Dethlefs, M. Fujii and O. Dopfer, *J. Phys. Chem. A*, 2010, **114**, 11139.
21 M. Schmies, A. Patzer, M. Fujii and O. Dopfer, *Phys. Chem. Chem. Phys.*, 2011, **13**, 13926.
22 M. Miyazaki, A. Takeda, M. Schmies, M. Sakai, K. Misawa, S. Ishiuchi, F. Michels, K. Müller-Dethlefs, O. Dopfer and M. Fujii, *Phys. Chem. Chem. Phys.*, 2014, **16**, 110.
23 H. S. Andrei, N. Solca and O. Dopfer, *Phys. Chem. Chem. Phys.*, 2004, **6**, 3801.
24 N. Solcà and O. Dopfer, *J. Phys. Chem. A*, 2002, **106**, 7261.
25 N. Solcà and O. Dopfer, *Eur. Phys. J. D*, 2002, **20**, 469.
26 Q. L. Gu and J. L. Knee, *J. Chem. Phys.*, 2008, **128**, 064311.
27 M. Schmies, A. Patzer, S. Kruppe, M. Miyazaki, S. Ishiuchi, M. Fujii and O. Dopfer, *ChemPhysChem*, 2013, **14**, 728.
28 T. Nakamura, M. Miyazaki, M. Weiler, M. Schmies, O. Dopfer and M. Fujii, *ChemPhysChem*, 2013, **14**, 741.
29 H. S. Andrei, N. Solca and O. Dopfer, *J. Phys. Chem. A*, 2005, **109**, 3598.
30 H. K. Gerardi, G. H. Gardenier, U. Viswanathan, S. M. Auerbach and M. A. Johnson, *Chem. Phys. Lett.*, 2011, **501**, 172.
31 N. Solcà and O. Dopfer, *Phys. Chem. Chem. Phys.*, 2004, **6**, 2732.
32 K. Sakota, M. Schütz, M. Schmies, R. Moritz, A. Bouchet, T. Ikeda, Y. Kuono, H. Sekiya and O. Dopfer, *Phys. Chem. Chem. Phys.*, 2014, **16**, 3798.
33 S. Ishiuchi, M. Sakai, Y. Tsuchida, A. Takeda, Y. Kawashima, M. Fujii, O. Dopfer and K. Müller-Dethlefs, *Angew. Chem., Int. Ed.*, 2005, **44**, 6149.
34 K. Tanabe, M. Miyazaki, M. Schmies, A. Patzer, M. Schütz, H. Sekiya, M. Sakai, O. Dopfer and M. Fujii, *Angew. Chem., Int. Ed.*, 2012, **51**, 6604.
35 C. Walter, R. Kritzer, A. Schubert, C. Meier, O. Dopfer and V. Engel, *J. Phys. Chem. A*, 2010, **114**, 9743.
36 M. Fujii and O. Dopfer, *Int. Rev. Phys. Chem.*, 2012, **31**, 131.
37 S. I. Ishiuchi, M. Sakai, Y. Tsuchida, A. Takeda, Y. Kawashima, O. Dopfer, K. Müller-Dethlefs and M. Fujii, *J. Chem. Phys.*, 2007, **127**, 114307.
38 M. Miyazaki, A. Takeda, S. Ishiuchi, M. Sakai, O. Dopfer and M. Fujii, *Phys. Chem. Chem. Phys.*, 2011, **13**, 2744.
39 S. Ishiuchi, M. Miyazaki, M. Sakai, M. Fujii, M. Schmies and O. Dopfer, *Phys. Chem. Chem. Phys.*, 2011, **13**, 2409.
40 K. Sakota, S. Harada, Y. Shimazaki and H. Sekiya, *J. Phys. Chem. A*, 2011, **115**, 626.
41 H. J. Wasserman, R. R. Ryan and S. P. Layne, *Acta Crystallogr., Sect. C: Cryst. Struct. Commun.*, 1985, **41**, 783.
42 Y. Baena, J. A. Pinzon, H. J. Barbosa and F. Martinez, *Phys. Chem. Liq.*, 2004, **42**, 603.
43 W. Caminati, A. Maris and A. Millemaggi, *New J. Chem.*, 2000, **24**, 821.
44 M. Miyazaki, J. Saikawa, H. Ishizuki, T. Taira and M. Fujii, *Phys. Chem. Chem. Phys.*, 2009, **11**, 6098.
45 V. P. Manea, K. J. Wilson and J. R. Cable, *J. Am. Chem. Soc.*, 1997, **119**, 2033.
46 S. Ullrich and K. Müller-Dethlefs, *J. Phys. Chem. A*, 2002, **106**, 9181.
47 C. Cabezas, M. Varela, W. Caminati, S. Mata, J. C. Lopez and J. L. Alonso, *J. Mol. Spectrosc.*, 2011, **268**, 42.
48 R. Nakagaki, T. Kobayashi and S. Nagakura, *Bull. Chem. Soc. Jpn.*, 1980, **53**, 901.
49 L. Klasinc, I. Novak, A. Sabljic and S. P. McGlynn, *Int. J. Quantum Chem.*, 1986, 251.
50 X. Tong, S. Ullrich, C. E. H. Dessent and K. Müller-Dethlefs, *Phys. Chem. Chem. Phys.*, 2002, **4**, 3578.
51 S. Ullrich and K. Müller-Dethlefs, *J. Phys. Chem. A*, 2002, **106**, 9188.
52 M. Weiler, T. Nakamura, H. Sekiya, O. Dopfer, M. Miyazaki and M. Fujii, *ChemPhysChem*, 2012, **13**, 3875.
53 O. Dopfer, *Int. Rev. Phys. Chem.*, 2003, **22**, 437.
54 P. J. Linstrom and W. G. Mallard, *NIST Chemistry WebBook*, National Institute for Standards and Technology, Gaithersburg MD, 20899, 2014, http://webbook.nist.gov.
55 M. J. Frisch, G. W. Trucks, H. B. Schlegel, G. E. Scuseria, M. A. Robb, J. R. Cheeseman, G. Scalmani, V. Barone, B. Mennucci, G. A. Petersson, H. Nakatsuji, M. Caricato, X. Li, H. P. Hratchian, A. F. Izmaylov, J. Bloino, G. Zheng, J. L. Sonnenberg, M. Hada, M. Ehara, K. Toyota, R. Fukuda, J. Hasegawa, M. Ishida, T. Nakajima, Y. Honda, O. Kitao, H. Nakai, T. Vreven, J. A. Montgomery Jr, J. E. Peralta, F. Ogliaro, M. Bearpark, J. J. Heyd, E. Brothers, K. N. Kudin, V. N. Staroverov, R. Kobayashi, J. Normand, K. Raghavachari, A. Rendell, J. C. Burant, S. S. Iyengar, J. Tomasi, M. Cossi, N. Rega, N. J. Millam, M. Klene, J. E. Knox, J. B. Cross, V. Bakken, C. Adamo, J. Jaramillo, R. Gomperts, R. E. Stratmann, O. Yazyev, A. J. Austin, R. Cammi, C. Pomelli, J. W. Ochterski, R. L. Martin, K. Morokuma, V. G. Zakrzewski, G. A. Voth, P. Salvador, J. J. Dannenberg, S. Dapprich, A. D. Daniels, Ö. Farkas, J. B. Foresman, J. V. Ortiz, J. Cioslowski and D. J. Fox, *GAUSSIAN09, Rev. A.02*, Gaussian, Inc., Wallingford CT, 2009.
56 M. D. Halls, J. Velkovski and H. B. Schlegel, *Theor. Chem. Acc.*, 2001, **105**, 413.
57 J. Cerny, X. Tong, P. Hobza and K. Müller-Dethlefs, *Phys. Chem. Chem. Phys.*, 2008, **10**, 2780.
58 D. Roth and O. Dopfer, *Phys. Chem. Chem. Phys.*, 2002, **4**, 4855.
59 N. Solcà and O. Dopfer, *Chem.–Eur. J.*, 2003, **9**, 3154.
60 E. J. Bieske and O. Dopfer, *Chem. Rev.*, 2000, **100**, 3963.
61 R. V. Olkhov and O. Dopfer, *Chem. Phys. Lett.*, 1999, **314**, 215.
62 O. Dopfer, D. Roth and J. P. Maier, *J. Am. Chem. Soc.*, 2002, **124**, 494.
63 P. Botschwina, R. Oswald and O. Dopfer, *Phys. Chem. Chem. Phys.*, 2011, **13**, 14163.

64 R. V. Olkhov, S. A. Nizkorodov and O. Dopfer, *J. Chem. Phys.*, 1997, **107**, 8229.
65 N. Solcà and O. Dopfer, *J. Am. Chem. Soc.*, 2004, **126**, 1716.
66 A. Patzer, M. Schütz, T. Möller and O. Dopfer, *Angew. Chem., Int. Ed.*, 2012, **51**, 4925.
67 O. Dopfer, H. S. Andrei and N. Solca, *J. Phys. Chem. A*, 2011, **115**, 11466.
68 A. Fujii, T. Ebata and N. Mikami, *J. Phys. Chem. A*, 2002, **106**, 10124.
69 S. A. Nizkorodov, O. Dopfer, M. Meuwly, J. P. Maier and E. J. Bieske, *J. Chem. Phys.*, 1996, **105**, 1770.
70 E. P. L. Hunter and S. G. Lias, *J. Phys. Chem. Ref. Data*, 1998, **27**, 413.
71 E. B. Wilson, *Phys. Rev.*, 1934, **45**, 706.
72 M. Schäfer and D. W. Pratt, *J. Chem. Phys.*, 2001, **115**, 11147.
73 O. Dopfer, *et al.*, unpublished results.